Theor. Comput. Fluid Dyn.
https://doi.org/10.1007/s00162-022-00616-z

ORIGINAL ARTICLE

Huaijin Yao · **Yiyang Sun** · **Maziar S. Hemati**

Feedback control of transitional shear flows: sensor selection for performance recovery

Received: 8 January 2022 / Accepted: 30 May 2022

Abstract The choice and placement of sensors and actuators is an essential factor determining the performance that can be realized using feedback control. This determination is especially important, but difficult, in the context of controlling transitional flows. The highly non-normal nature of the linearized Navier–Stokes equations makes the flow sensitive to small perturbations, with potentially drastic performance consequences on closed-loop flow control. Full-information controllers, such as the linear quadratic regulator (LQR), have demonstrated some success in reducing transient energy growth and suppressing transition; however, sensor-based output feedback controllers with comparable performance have been difficult to realize. In this study, we propose two methods for sensor selection that enable sensor-based output feedback controllers to recover full-information control performance: one based on a sparse controller synthesis approach, and one based on a balanced truncation procedure for model reduction. Both approaches are investigated within linear and nonlinear simulations of a sub-critical channel flow with blowing and suction actuation at the walls. We find that sensor configurations identified by both approaches allow sensor-based static output feedback LQR controllers to recover full-information LQR control performance, both in reducing transient energy growth and suppressing transition. Further, our results indicate that both the sensor selection methods and the resulting controllers exhibit robustness to Reynolds number variations.

Keywords Sensor selection · Transient growth · Static output feedback · Flow control

1 Introduction

Preventing or delaying transition to turbulence via flow control is a topic of great technological interest. At a sufficiently high Reynolds number, a flow will transition from a low-skin-friction laminar regime to a high-skin-friction turbulent regime. For many wall-bounded shear flows, a sub-critical transition can arise due to non-modal instabilities [1,2]. The high degree of non-normality of the linearized Navier–Stokes equations can cause flow perturbations to exhibit large peaks in kinetic energy, even when the flow is linearly stable. This so-called *transient energy growth (TEG)* of flow perturbations serves as a driving mechanism for sub-critical transition. TEG causes large deviations of the flow state from the laminar equilibrium, pushing it outside the

H. Yao (✉) · S. Hemati (✉)
Aerospace Engineering and Mechanics, University of Minnesota, Minneapolis 55455, MN, USA
E-mail: yaoxx368@umn.edu

M. S. Hemati
E-mail: mhemati@umn.edu

Y. Sun
Mechanical and Aerospace Engineering, Syracuse University, Syracuse 13244, NY, USA
E-mail: ysun58@syr.edu

Published online: 25 June 2022

basin of attraction and triggering secondary instabilities that ultimately transition the flow to turbulence [3–8]. An ability to reduce TEG—e.g., using flow control—could provide a means of suppressing transition to turbulence.

In studying TEG, it is important to note that not all flow perturbations will trigger transient growth, and so it is important to consider "optimal" or "worst-case" perturbations that give rise to the maximum TEG for a fixed perturbation amplitude [9]. Considerations of worst-case performance are especially important when investigating and comparing the performance of different flow control strategies that aim to reduce TEG and suppress transition to turbulence. The optimal disturbance for the uncontrolled flow will not necessarily be the same as the optimal disturbance for the controlled flow. These optimal disturbances will vary further depending on the specific control design and may even involve perturbations in the control system dynamics due to various sources of uncertainty [10]. Comparing worst-case performance ensures that comparisons of control performance remain fair.

Feedback control has been proposed as a way to reduce TEG and suppress transition in a number of flow configurations. Such approaches to flow control rely upon a control law (algorithm) to process available sensor measurements and determine an appropriate control action by the actuation. Within numerical simulations, the linear quadratic regulator (LQR) has shown some success in reducing TEG and delaying transition in shear-flows using wall blowing and suction actuation [11–14]. LQR controllers are designed to minimize a balance between flow perturbation energy and control effort. LQR control is an attractive choice because of its simplicity, but also because these controllers robustly reduce TEG in the face of parameter uncertainties (e.g., Reynolds number variations) [15]. Unfortunately, LQR controllers require full-state information that can be difficult to access outside of numerical simulations. For incompressible flows, full-state information corresponds to measurements of the entire velocity and/or vorticity field. Instead, sensor-based output feedback controllers are required to act based on partial information. In principle, one can adopt an observer-based feedback approach, wherein measurements from a limited set of sensors are used to first estimate the full state of the flow, and to then apply a full-state feedback control law to these estimates. Unfortunately, such approaches can exhibit degraded TEG performance if not properly designed [10,16]. Although sophisticated estimation strategies can be devised to overcome some of these performance issues [17,18], these strategies have not been shown to recover full-information control performance.

Static output feedback controllers have been proposed as a convenient design alternative to observer-based feedback control [10,16]. Static output feedback LQR (SOF-LQR) control, in particular, can be designed using the same objective function as the full-information LQR controller, but with a constraint that the controller acts as a direct feed-through from the measured sensor-outputs to commanded inputs [19–22]. This feed-through structure ensures that SOF-LQR controllers satisfy a necessary condition for TEG elimination [10,23]. In previous studies [16,22,24], we have found that SOF using wall-based shear–stress sensing is able to reduce TEG, but as with LQG controllers, these control laws are unable to recover the same worst-case performance as the full-information LQR counterpart. This is not entirely surprising, as the achievable performance of a control law is intimately tied to the specific choice of actuators and sensors implemented for control. Thus, the specific choice and arrangement of sensors is an important consideration in the design of sensor-based output feedback control strategies.

A number of studies have considered the problems of sensor selection for flow reconstruction [25–30] and actuator selection for flow control [31–34]. Sensor selection for flow reconstruction has been of particular interest because it can benefit the design of flow estimation and diagnostic strategies. However, in the context of TEG and transition control, even a "perfect" flow estimator can result in degraded control performance when the estimator design is decoupled from the design of the control law [10]. Here, we are interested in selecting a set of sensors that enables sensor-based output feedback control to achieve comparable performance as a full-state feedback controller. In particular, we aim to do this in the context of TEG reduction and transition control, without resorting to flow reconstruction and observer-based feedback designs.

In this paper, we propose two approaches for sensor selection that enable performance recovery of sensor-based output feedback controllers. Both approaches are formulated as down-selection problems from a library of candidate sensors. In this proof-of-concept investigation, we consider a library of candidate velocity sensors distributed throughout the interior of a channel flow. One approach leverages the fact that full-information LQR and SOF-LQR controllers can be made equivalent when the library of candidate sensors is sufficiently rich. Thus, the controller gain for the associated SOF-LQR controller can be evaluated to determine the relative contribution of each candidate sensor to the control performance. In doing so, sensors with little contribution to control actions can be identified and discarded to yield a sparse set of sensors without sacrificing flow control performance. The second approach is based on ideas from linear model reduction using balanced truncation.

Balanced truncation yields a low-dimensional model that maintains the input–output dynamics of the system. The low-order representation of the state-space for these reduced-order models also exposes redundant signals from sensors in the candidate library. These redundant sensors can be identified and removed using a pivoted QR decomposition to yield a sparse set of sensors for SOF-LQR controller synthesis. We find that both of these approaches identify sensor configurations that allow SOF-LQR to recover full-state LQR TEG performance within linear simulations of a channel flow with wall-normal blowing and suction actuation. Each approach identifies a different configuration of velocity sensors distributed along the interior of the channel. We further evaluate the control performance using direct numerical simulations (DNS) of a nonlinear channel flow. DNS are performed with various optimal disturbance amplitudes to examine the nonlinear effects and the control mechanism that delays or suppresses the laminar-to-turbulent transition.

The paper is organized as follows: In Sect. 2, we present the linearized channel flow model and an overview of relevant controller synthesis approaches. In Sect. 3, we formulate two approaches for sensor selection that can be used for flow control performance recovery. Section 4 presents sensor configurations and linear performance analysis results for a sub-critical channel flow. This is followed by nonlinear performance results from direct numerical simulations of a sub-critical channel flow in Sect. 5. Finally, we draw conclusions in Sect. 6.

2 Channel flow model and control synthesis

2.1 Channel flow

We consider plane Poiseuille flow at sub-critical Reynolds number of $Re = \bar{\boldsymbol{u}}_{\boldsymbol{c}} h/\nu = 3000$ defined by the centerline velocity of the base flow $\bar{\boldsymbol{u}}_{\boldsymbol{c}}$, half height of the channel h, and kinematic viscosity ν. As shown in Fig. 1, the velocity profile of the base flow is $[\bar{\boldsymbol{u}}, \bar{\boldsymbol{v}}, \bar{\boldsymbol{w}}] = [1 - (y/h)^2, 0, 0]$ with coordinate origin at the center line between walls, where $\bar{\boldsymbol{u}}$, $\bar{\boldsymbol{v}}$, $\bar{\boldsymbol{w}}$ represent velocity components in streamwise x, wall-normal y, and spanwise z directions, respectively. The parabolic profile of the velocity is the laminar equilibrium solution of the flow. In this study, length-scale variables are non-dimensionalized by the channel half-height h, and velocities are non-dimensionalized by the centerline velocity of base flow $\bar{\boldsymbol{u}}_{\boldsymbol{c}}$. Time is denoted by t.

The flow at this condition is linearly stable, since there are no unstable modes from the linear stability analysis. However, a large transient energy growth of small perturbations is observed at this flow condition, and a laminar-to-turbulent transition emerges as a result of certain flow perturbations. Hence, our objective is to design feedback control strategies to suppress the transient energy growth and further prevent the emergence of laminar-to-turbulent transition.

The flow control configuration is illustrated in Fig. 1. We introduce actuation in the form of blowing and suction in the wall-normal direction on the upper and lower channel walls. The velocity profile of the actuation is spatially periodic in the streamwise and spanwise directions, in accordance with the channel flow model discussed below. In this study, we consider velocity sensors along the channel interior, but the methods we introduce are valid equally with wall-based sensing as well.

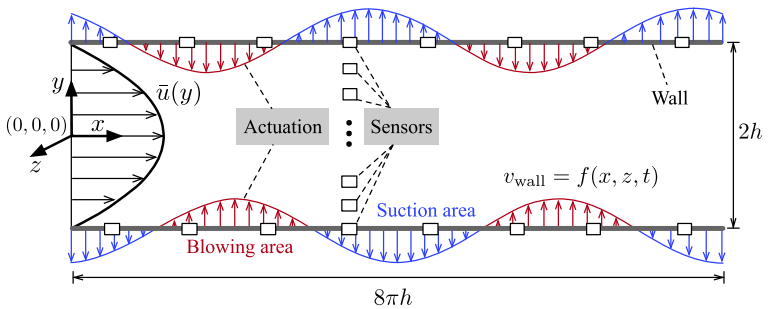

Fig. 1 Schematic of plane Poiseuille flow and implementation of sensing and actuation used for flow control (not to scale)

2.2 Linearized Navier–Stokes equations

We decompose the flow state $\boldsymbol{q}$ into base state $\bar{\boldsymbol{q}}$ and small perturbation $\boldsymbol{q}'$ ($\boldsymbol{q} = \bar{\boldsymbol{q}} + \boldsymbol{q}'$), where $\boldsymbol{q} = [\boldsymbol{u}, \boldsymbol{v}, \boldsymbol{w}, \boldsymbol{p}]^{\mathsf{T}}$ ($\boldsymbol{p}$ is pressure), and $(\cdot)^{\mathsf{T}}$ represents transpose. The kinetic energy density of a perturbation is defined as,

$$E = \frac{1}{2V}\int_V (\boldsymbol{u}'^2 + \boldsymbol{v}'^2 + \boldsymbol{w}'^2)\mathrm{d}V, \tag{1}$$

where V is the volume of the computational domain.

By substituting the expression of $\boldsymbol{q} = \bar{\boldsymbol{q}} + \boldsymbol{q}'$ into the Navier–Stokes equations, and assuming that the perturbation is much smaller than the base state in magnitude ($|\boldsymbol{q}'| \ll |\bar{\boldsymbol{q}}|$), we linearize the equations by retaining linear terms and neglecting higher-order nonlinear terms as follows,

$$\begin{aligned}
\frac{\partial \boldsymbol{u}'}{\partial x} + \frac{\partial \boldsymbol{v}'}{\partial y} + \frac{\partial \boldsymbol{w}'}{\partial z} &= 0 \\
\frac{\partial \boldsymbol{u}'}{\partial t} + \bar{\boldsymbol{u}}\frac{\partial \boldsymbol{u}'}{\partial x} + \boldsymbol{v}'\frac{\partial \bar{\boldsymbol{u}}}{\partial y} &= \frac{\partial \boldsymbol{p}'}{\partial x} + \frac{1}{Re}\nabla^2 \boldsymbol{u}' \\
\frac{\partial \boldsymbol{v}'}{\partial t} + \bar{\boldsymbol{u}}\frac{\partial \boldsymbol{v}'}{\partial x} &= \frac{\partial \boldsymbol{p}'}{\partial y} + \frac{1}{Re}\nabla^2 \boldsymbol{v}' \\
\frac{\partial \boldsymbol{w}'}{\partial t} + \bar{\boldsymbol{u}}\frac{\partial \boldsymbol{w}'}{\partial x} &= \frac{\partial \boldsymbol{p}'}{\partial z} + \frac{1}{Re}\nabla^2 \boldsymbol{w}'.
\end{aligned} \tag{2}$$

The linearized Navier–Stokes equations are further manipulated to be expressed in terms of wall-normal velocity $\boldsymbol{v}'$ and wall-normal vorticity $\boldsymbol{\eta}'$ as described in [1] as,

$$\begin{aligned}
\frac{\partial(\nabla^2 \boldsymbol{v}')}{\partial t} + \bar{\boldsymbol{u}}\frac{\partial(\nabla^2 \boldsymbol{v}')}{\partial x} - \frac{\partial^2 \bar{\boldsymbol{u}}}{\partial y^2}\frac{\partial \boldsymbol{v}'}{\partial x} - \frac{1}{Re}\nabla^2(\nabla^2 \boldsymbol{v}') &= 0 \\
\frac{\partial \boldsymbol{\eta}'}{\partial t} + \frac{\partial \bar{\boldsymbol{u}}}{\partial y}\frac{\partial \boldsymbol{v}'}{\partial z} + \bar{\boldsymbol{u}}\frac{\partial \boldsymbol{\eta}'}{\partial x} - \frac{1}{Re}\nabla^2 \boldsymbol{\eta}' &= 0.
\end{aligned} \tag{3}$$

Next, the real-valued three-dimensional perturbation of wall-normal velocity and wall-normal vorticity are expressed using Fourier expansions in the homogeneous x- and z-directions,

$$\begin{aligned}
\boldsymbol{v}'(x, y, z, t) &= \hat{\boldsymbol{v}}(y, t)e^{i(\alpha x + \beta z)} + \text{complex conjugate}, \\
\boldsymbol{\eta}'(x, y, z, t) &= \hat{\boldsymbol{\eta}}(y, t)e^{i(\alpha x + \beta z)} + \text{complex conjugate},
\end{aligned} \tag{4}$$

where $\hat{\boldsymbol{v}}(y, t)$ and $\hat{\boldsymbol{\eta}}(y, t)$ are amplitude functions of the perturbation associated with streamwise wavenumber α and spanwise wavenumber β. By plugging (4) into the linearized Navier–Stokes equations (2), we obtain the Orr–Sommerfeld and Squire equations as follows,

$$\begin{bmatrix} \dot{\hat{\boldsymbol{v}}} \\ \dot{\hat{\boldsymbol{\eta}}} \end{bmatrix} = \begin{bmatrix} -i\alpha\bar{\boldsymbol{u}} + \frac{i\alpha\bar{\boldsymbol{u}}_{yy}}{(\mathcal{D}^2 - k^2)} + \frac{1}{Re}(\mathcal{D}^2 - k^2) & 0 \\ -i\beta\bar{\boldsymbol{u}}_y & -i\alpha\bar{\boldsymbol{u}} + \frac{1}{Re}(\mathcal{D}^2 - k^2) \end{bmatrix} \begin{bmatrix} \hat{\boldsymbol{v}} \\ \hat{\boldsymbol{\eta}} \end{bmatrix}, \tag{5}$$

where $\mathcal{D}$ represents differentiation with respect to the wall-normal direction y, $\bar{\boldsymbol{u}}_y$ and $\bar{\boldsymbol{u}}_{yy}$ denote the first and second derivatives of $\bar{\boldsymbol{u}}$ with respect to y, and $k^2 := \alpha^2 + \beta^2$. The governing equations (5) are in a state-space form

$$\frac{\partial X_u(y)}{\partial t} = A_u(\bar{\boldsymbol{q}}; \alpha, \beta)X_u(y), \tag{6}$$

where $X_u = [\hat{\boldsymbol{v}}, \hat{\boldsymbol{\eta}}]^{\mathsf{T}}$ is the state, and subscript $(\cdot)_u$ indicates uncontrolled system.

In the y-direction, flow variables are represented by Chebyshev polynomials with $N = 101$ discrete collocation points, and a no-slip boundary condition is prescribed at the upper and lower walls for the uncontrolled baseline flow, i.e., $\hat{\boldsymbol{v}}(\pm h) = \hat{\boldsymbol{v}}_y(\pm h) = \hat{\boldsymbol{\eta}}(\pm h) = 0$.

In the control design, we introduce actuation in the form of wall-normal blowing and suction at the upper and lower channel walls (see Fig. 1). This actuation modifies the uncontrolled dynamic system (6) to form a controlled dynamical system

$$\frac{\partial X}{\partial t} = AX + BU, \tag{7}$$

where A is the system matrix, X is the state, U is the input, and B is the input matrix that maps the influence of control inputs to the state evolution. Here the control input is selected to be $U = \frac{\partial}{\partial t}[\hat{\boldsymbol{v}}\ |_{+h}, \hat{\boldsymbol{v}}\ |_{-h}]^T$, representing the rate of change of wall-normal velocity on the upper and lower walls. Since the control input U represents the change of Fourier coefficients of wall-normal velocity $\hat{\boldsymbol{v}}$, in Fig. 1 it is shown in the form of a sinusoidal wave. The no-flow-through boundary conditions ($\hat{\boldsymbol{v}}\ |_{\pm h} = 0$) are excluded from X_u in (6). In the controlled case, $\hat{\boldsymbol{v}}\ |_{\pm h}$ are nonzero, so we append these two state variables to the flow state X_u to form a new state $X = [X_u, \hat{\boldsymbol{v}}\ |_{+h}, \hat{\boldsymbol{v}}\ |_{-h}]^{\mathsf{T}}$. Analogously, the dynamics matrix A_u is modified and denoted by A to account for the new state.

In all that follows, we transform all quantities to their equivalent real-valued representations so that $A \in \mathbb{R}^{n\times n}$, $X \in \mathbb{R}^n$, $B \in \mathbb{R}^{n\times m}$, and $U \in \mathbb{R}^m$. Further, all measured sensor outputs $Y \in \mathbb{R}^p$ to be considered in this study will be represented by the output equation

$$Y(t) = CX(t). \tag{8}$$

Further details about the model formulation can be found in [35].

2.3 Transient energy growth and control synthesis

In this study, we aim to use feedback control to reduce the transient energy growth (TEG). We consider TEG due to some initial flow perturbation $X(t_0) = X_0$.

The associated system response is given by $X(t) = \mathrm{e}^{A(t-t_0)}X_0$, and the associated perturbation kinetic energy is given as,

$$E(t) = X^{\mathsf{T}}(t)QX(t), \tag{9}$$

where $Q = Q^{\mathsf{T}} > 0$. Further, the maximum TEG is defined as,

$$G = \max_{t\geq t_0} \max_{E(t_0)\neq 0} \frac{E(t)}{E(t_0)}, \tag{10}$$

which results from a so-called *worst-case* or *optimal perturbation* [36]. The system can exhibit TEG whenever $G > 1$. In this study, we always evaluate the maximum TEG for a given system. The worst-case perturbations are calculated using the algorithm proposed in [37], which performs a bisection over an iteratively refined time interval to determine the optimal perturbation to arbitrary accuracy. We emphasize that, in general, perturbation for the uncontrolled flow will be different from the one for the controlled flow, and so these perturbations must be determined independently.

To use feedback control to achieve TEG reduction, the control input vector U at a given instant is determined from available system information. For a full-state feedback control, the state X is assumed to be known and available for feedback, i.e., full-information control:

$$U(t) = KX(t), \tag{11}$$

where the design variable $K \in \mathbb{R}^{m\times n}$ is called the state feedback gain matrix.

LQR synthesis is based on solving,

$$\min_{U(t)} J = \int_0^\infty X^{\mathsf{T}}(t)QX(t) + U^{\mathsf{T}}(t)RU(t)\mathrm{d}t \tag{12}$$

subject to the linear dynamic constraint given in (7), where $R > 0$. The resulting full-state feedback LQR controller gain matrix K is determined from the solution of an algebraic Riccati equation [38]. Although LQR controllers will not necessarily minimize TEG, they have been shown to reduce TEG in shear flows and to exhibit robustness to parametric uncertainties [12–14].

Outside of numerical simulations, it can be challenging to obtain the full velocity and/or vorticity field information in an efficient manner. This makes it difficult to obtain full-state information as required for performing full-state feedback controller. In order to achieve feedback control with the measured information from sensors, in this study, we propose to use a static output feedback (SOF) control structure. For SOF control, the control input is determined directly from the measured output Y in an analogous manner to full-state feedback, with

$$U(t) = FY(t), \tag{13}$$

where the design variable $F \in \mathbb{R}^{m\times p}$ is called the SOF feedback gain matrix. The SOF form of LQR control was proposed for TEG control in [16,22]. The SOF-LQR solves the same minimization problem as shown in (12), but with an SOF constraint on the feedback law. This is equivalently written as,

$$J = \int_0^\infty X^\mathsf{T}(t)[Q + (FC)^\mathsf{T} R(FC)]X(t)\mathrm{d}t. \tag{14}$$

The SOF-LQR can be solved using iterative Anderson–Moore methods [20,39]. In this study, we use the Anderson–Moore algorithm with Armijo-type adaptation proposed in [16]. The details are given in "Appendix A." Additionally, the input weighting matrix R in this study is chosen to be $R = 10^{-6}I$, which removes the penalty on control in the objective function and emphasizes flow regulation over control efficiency in the controller designs.

3 Sensor selection for state feedback performance recovery

In this section, we propose two methods for selecting a sparse set of sensors to enable sensor-based SOF controllers to recover full-information control performance. We restrict the discussion to sensor selection and linear quadratic performance, but the approach is applicable more generally and can be used for actuator selection and other performance measures just as well.

The basic idea begins by recognizing that SOF-LQR control can be made equivalent to full-information LQR control if an available set of $p \geq n$ sensors is *sufficiently rich*. Here, the term *sufficiently rich* amounts to requiring the output matrix to have full column rank (i.e., $C = C_n \in \mathbb{R}^{p\times n}$ with $\mathrm{rank}(C_n) = n$). Since the closed-loop dynamics for SOF-LQR control are given by

$$\dot{X}(t) = (A + BF_nC_n)X(t), \tag{15}$$

it follows that the SOF-LQR gain F_n can be designed from the full-state feedback LQR gain K to recover full-state feedback LQR performance exactly: simply find a gain F_n that satisfies $F_nC_n = K$. From this insight, it follows that if we form a sufficiently rich library of candidate sensors, then the sensor selection problem can be recast as a problem of sensor down-selection. That is, given a sufficiently rich library of sensors, we aim to determine which sensors can be removed from the library such that the closed-loop performance of the controlled system (15) will be minimally impacted. Doing so will result in a sparse set of $r < n$ sensors with associated output matrix $C_r \in \mathbb{R}^{r\times n}$. The general problem of optimal sensor selection for state feedback performance recovery is non-convex and combinatorially hard to solve. Here, we propose two heuristic methods for overcoming this challenge to achieve performance recovery via sensor down-selection from a sufficient rich library of candidate sensors: one based on controller gain evaluation (see section 3.1), and another based on a balanced truncation procedure (see section 3.2). These methods are motivated by sparse control synthesis [40,41] and greedy Gramian-based optimization methods [27,34], respectively. Both methods will make it possible for SOF-LQR controllers to recover full-state LQR performance, as will be demonstrated in Sects. 4 and 5 . In this work, we focus on velocity sensors for simplicity. However, other (heterogeneous) sensor libraries can be used just the same. We also emphasize that any sensor type/location constraints should be considered in the construction of the library—i.e., only permissible sensors should be included in the library.

3.1 Sensor selection by column-norm evaluation (CE)

The first approach we propose is motivated by sparse controller synthesis techniques [40,41], by which a convex optimization problem is posed to solve for a controller gain that achieves the performance objective

while balancing either row- or column-sparsity in the resulting controller gain. Due to the computational complexity of generic off-the-shelf solvers, these sparse synthesis methods tend to require specialized and dedicated solvers for high-dimensional system such as fluid flows. As such, rather than working with this optimization problem directly, here propose a heuristic approach that is comparatively simpler to implement.

The basic approach we propose stems from the fact that a controller gain matrix contains important information regarding the relative contribution of individual sensors and actuators to the controlled closed-loop dynamics in (15). If we design a controller gain F_n based on a sufficiently rich library of candidate sensors, then each column in F_n corresponds to a specific sensor in the candidate library, represented as a row of C_n. Thus, by evaluating the relative norm of each column in F_n, we can determine the relative contribution of a particular sensor to the control action and the closed-loop dynamics in (15). Here, we assess the relative importance of sensors by evaluating the relative L_2-norm of each column in the gain matrix F_n. Let $F_n(:, i)$ indicate the ith column of F_n, then the L_2-norm is calculated as

$$\| F_n(:, i) \|_2 = \sqrt{\sum_{j=1}^{n} F_n(j, i)^2}, \tag{16}$$

where $F_n(j, i)$ is the jth element of the ith column of F_n. Consider, for example, that a column in F_n of all zeros and the associated row in C_n could be removed completely without altering the closed-loop system response in (15). In general, columns of F_n with large norm contribute more to the closed-loop response than the columns of F_n with small norm. Thus, the rows in C_n associated with the dominant columns in F_n indicate sensors that are "more important" for the controlled system dynamics. Therefore, we identify the subset of r columns with the largest relative norm, denoted by their indices $j_1, \cdots, j_r$. Then, a new output matrix C_r containing a reduced set of r sensors can be constructed from the rows $j_1, \cdots, j_r$ of C_n. In principle, a gain matrix F_r for this reduced set of sensors can be determined directly from the columns $j_1, \cdots, j_r$ of F_n, but it is actually beneficial to compute an optimal gain F by re-designing the SOF gain for the system (A, B, C_r). In the present work, we consider linear quadratic control objectives, so the re-design is performed based on SOF-LQR synthesis via an iterative Anderson–Moore algorithm (see "Appendix A").

The method proposed here for sensor selection by column-norm evaluation (CE) is summarized in Algorithm 4. Note that it can be useful to scale the outputs of the candidate sensor library so that each row of C_n has unit norm. This results from the fact that the scaling of the sensor output is inversely associated with the scale of the associated column norm in F_n. Performing this scaling to unit norm output tends to be important when a heterogeneous set of sensors is used to construct the candidate library (e.g., velocity, pressure, and shear–stress); otherwise, the importance of a particular type of sensor can be artificially inflated or deflated by the nature of observable quantity itself. A justification for the CE approach for sensor selection is presented by means of an illustrative example in "Appendix B".

Lastly, note that a similar procedure to Algorithm 4 can be formulated for actuator selection by considering the relative norm of rows in F_n, each corresponding to an actuator represented as a column of the input matrix B in (15). Step 0 in this "actuator selection by row-norm evaluation" would then be to match full-information control performance $B_n F_n = K$ using a sufficiently rich library of candidate actuators B_n. The remaining steps in Algorithm 4 would then follow analogously, replacing "sensors" with "actuators," all "C" matrices with "B" matrices, and also interchanging all references to "rows" with "columns" and "columns" with "rows." We note again that these ideas are closely related to sparse controller synthesis techniques based on convex optimization, which can be used to explicitly promote sparsity and design controller gains with many columns or rows of all zeros [40,41].

Algorithm 1: ***Sensor selection by column-norm evaluation (CE)***

step 0: Form a sufficiently rich library of candidate sensors C_n, and design an SOF controller F_n that achieves the same performance as the desired full-information controller by solving $F_n C_n = K$.
step 1: Evaluate the L_2-norm of each column in F_n, then save the indices $\{j_1, \cdots, j_r\}$ of the r columns with the largest relative L_2-norm.
step 2: Construct a reduced measurement matrix C_r whose r rows consist of rows $j_1, \cdots, j_r$ of C_n.
step 3: Re-design an SOF controller based on (A, B, C_r).

3.2 Sensor selection by balanced truncation

Another sensor selection procedure can be devised using the notion of balanced truncation [42–44]. Balanced truncation is a model reduction method for linear systems that works by truncating states with a lesser contribution to a system's input–output dynamics. To do so, the state-space is first transformed into balanced coordinates $\bar{X}_b = TX$, so that the controllability Gramian W_c and the observability Gramian W_o are equal and diagonal. That is, in balanced coordinates we have $\bar{W}_c = \bar{W}_o = \text{diag}(\sigma_1, \cdots, \sigma_n)$, where $\sigma_1 \geq \sigma_2 \geq \cdots \geq \sigma_n$ are the system's Hankel Singular Values (HSVs). Larger HSVs indicate directions of state-space with greater contribution to the input–output dynamics, whereas smaller HSVs indicate directions of state-space with lesser contribution to the input–output dynamics. As such, truncation in balanced coordinates of the $n-r$ states with the smallest HSVs will allow a reduction to an r-dimensional state-space, while preserving information that is most important for capturing the input–output dynamics. This idea can be extended for sensor selection from a sufficiently rich library of candidate sensors C_n, since a reduction to an r-dimensional state-space will necessarily lead to an output matrix with redundant rows. Upon eliminating these redundant rows in C_n—e.g., by means of a pivoted QR decomposition—we will be left with r linearly independent rows (sensors) that are relevant for feedback control. The basic approach here boils down to a greedy selection procedure for Gramian-based optimization and $\mathcal{H}_2/\mathcal{H}_\infty$ performance objectives [27,34].

The balancing transformation can be determined by first computing the system Gramians from the associated Lyapunov equations,

$$\begin{aligned} AW_c + W_cA^T + BB^T &= 0 \\ W_oA + A^TW_o + C_n^TC_n &= 0. \end{aligned} \tag{17}$$

Then, using the lower triangular Cholesky factorizations L_o and L_c of W_o and W_c, respectively, and the singular value decomposition of their product $L_o^TL_c = \Phi\Sigma\Psi^T$, the balancing transformation can be computed as

$$\begin{aligned} T &= L_c\Psi\Sigma^{\frac{1}{2}} \\ T^{-1} &= \Sigma^{\frac{1}{2}}\Phi^TL_o^T. \end{aligned} \tag{18}$$

By retaining the r states with the largest HSVs and truncating the rest, the reduced-order system resulting from balanced truncation can be expressed as

$$\begin{aligned} \dot{X}_b(t) &= A_bX_b(t) + B_bU(t) \\ Y_b(t) &= C_bX_b(t), \end{aligned} \tag{19}$$

where $A_b \in \mathbb{R}^{r\times r}$, $B_b \in \mathbb{R}^{r\times m}$, $C_b \in \mathbb{R}^{p\times r}$, the reduced-order state $X_b \in \mathbb{R}^r$, input vector $U \in \mathbb{R}^m$, and output vector $Y_b \in \mathbb{R}^p$. Since $r < n$, the output matrix C_b will necessarily have redundant rows. Thus, only r linearly independent rows (sensors) are needed to achieve the same feedback control performance as the reduced-order system with the full sensor library. To see this, consider that the static output feedback control determines the control action directly from the measured output as $U = F_nY_n$. This can be approximately achieved based on the reduced-order model attained via balanced truncation as $U = F_nY_n \approx F_nY_b$ (see Fig. 2). Now, since $Y_b = C_bX_b$ and C_b has redundant rows, it is possible to exactly reproduce this control signal from a reduced set of r outputs $Y_r = C_sX_b$ with $C_s \in \mathbb{R}^{r\times r}$ as $U = F_nY_b = F_rY_r$. This final output signal can be represented in the original basis for the full n-dimensional state-space, which determines the specific sensors that are needed to recover full-information feedback control performance using output feedback control.

In order to down-select to a set of r linearly independent rows from the output matrix C_b, we make use of the column-pivoted QR decomposition as

$$C_b^{\mathsf{T}}\mathbf{E} = \mathbf{QR}, \tag{20}$$

where $\mathbf{Q} \in \mathbb{R}^{r\times r}$ is an orthogonal matrix and $\mathbf{R} \in \mathbb{R}^{r\times p}$ is an upper triangular matrix with diagonal elements r_{ii}, with $|\ r_{11}\ | \geq |\ r_{22}\ | \geq \cdots \geq |\ r_{nn}\ |$. The independent rows $j_1, \cdots, j_r$ of C_b can be identified by entries in the column permutation matrix $\mathbf{E} \in \mathbb{R}^{p\times p}$. Thus, only these rows of C_b are retained in order to down-select the number of sensors and obtain the associated output matrix C_s shown graphically in Fig. 2c. Similarly, these same indices can be used to construct the output matrix C_r in the original n-dimensional basis for the state-space: simply construct C_r from rows $j_1, \cdots, j_r$ of C_n. All that remains at this point is to re-design

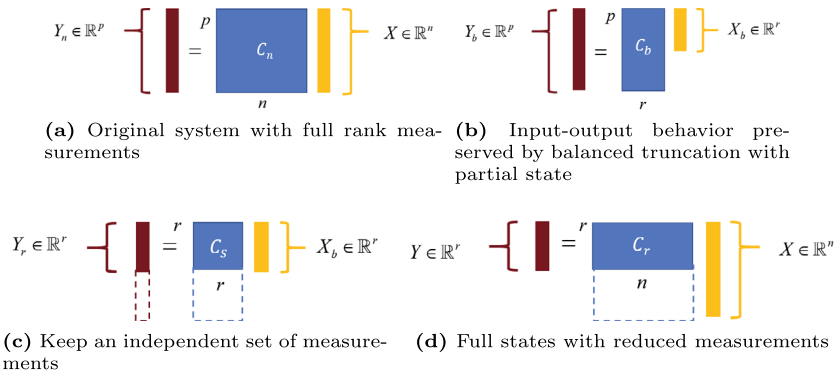

(a) Original system with full rank measurements

(b) Input-output behavior preserved by balanced truncation with partial state

(c) Keep an independent set of measurements

(d) Full states with reduced measurements

Fig. 2 Illustration of measurement selection by balanced truncation

an SOF controller based on the system (A, B, C_r) that uses this reduced set of sensors. A summary of this balanced truncation (BT) sensor selection approach is summarized as Algorithm 2. Note that, as with the CE sensor selection approach, this BT approach can be formulated analogously for actuator selection as well, again by solving the dual problem. That is, step 0 in this "actuator selection by balanced truncation" would then be modified to form a sufficiently rich library of candidate actuators B_n, then replacing all "C" matrices with "B" matrices and interchanging all references to "rows" with "columns" and "columns" with "rows." The only subtle difference in the actuator selection algorithm would arise in step 3, where the column-pivoted QR factorization of B_b would be used (or the row-pivoted QR factorization of B_b^{T}. Similar ideas for using balanced model reduction methods for sensor and actuator selection have been investigated in [27].

The choice of r in the carrying out the above steps to is important for ensuring that the final sensor configuration is able to achieve the desired control performance. One way to make this determination is to evaluate the difference between the input–output dynamics of the r-dimensional reduced-order balanced truncation model relative to the n-dimensional full-order model. We can evaluate this error by first defining an error system Σ_e that maps any input U to the associated error at the output $e = Y_n - Y_b$:

$$\begin{aligned} \begin{bmatrix} \dot{X}(t) \\ \dot{X}_b(t) \end{bmatrix} &= \begin{bmatrix} A & 0 \\ 0 & A_b \end{bmatrix} \begin{bmatrix} X(t) \\ X_b(t) \end{bmatrix} + \begin{bmatrix} B \\ B_b \end{bmatrix} U(t) \\ e(t) &= \begin{bmatrix} C_n & -C_b \end{bmatrix} \begin{bmatrix} X(t) \\ X_b(t) \end{bmatrix}. \end{aligned} \tag{21}$$

Then, an appropriate r can be determined by evaluating an associated system norm of Σ_e and ensuring it falls below some threshold err. A small system norm when the error system holds small system norms, the ROM captures the original system's input–output dynamics well. In this study, we can consider both the $\mathcal{H}_2$- and $\mathcal{H}_\infty$-norms of Σ_e. The $\mathcal{H}_2$-norm of Σ_e is denoted as $\|\Sigma_e\|_{\mathcal{H}_2}$ and corresponds to the root-mean-square of the impulse response of Σ_e. The $\mathcal{H}_\infty$-norm of Σ_e is denoted by $\|\Sigma_e\|_{\mathcal{H}_\infty}$ and corresponds to the peak value of the largest singular value of Σ_e.

Algorithm 2: ***Sensor selection by balanced truncation (BT)***

step 0: Form a sufficiently rich library of candidate sensors C_n.
step 1: Transform the system (A, B, C_n) to balanced coordinates using the balancing transformation in (18).
step 2: Perform a balanced truncation to the r-dimensional system representation in (19), with associated output matrix C_b.
step 3: Perform a column-pivoted QR factorization of C_b^{T} as in (20) to identify a set of r linearly independent rows $\{j_1, \cdots, j_r\}$ from C_b.
step 4: Construct a new output matrix C_r from rows $\{j_1, \cdots, j_r\}$ of the original candidate library of sensors C_n. This C_r represents the sparse sensor configuration.
step 5: Design an SOF controller based on the system (A, B, C_r).

4 Results: sensor selection and linear performance analysis

In the previous section, we proposed two approaches for sensor selection—one based on column-norm evaluation (CE) and one based on balanced truncation (BT)—that can enable a sensor-based SOF controller to recover full-information control performance. Here, we apply each method for sensor-based output feedback control of the linearized channel flow with $Re = 3000$ described in Sect. 2.1. The SOF-LQR controllers here will be designed to recover the full-information LQR control TEG performance subject to worst-case streamwise $(\alpha, \beta) = (1, 0)$, oblique $(\alpha, \beta) = (1, 1)$, and spanwise $(\alpha, \beta) = (0, 2)$ disturbances.[1] Sensors will be determined from a sufficiently rich library of velocity sensors, distributed at Chebyshev collocation points along the wall-normal direction throughout the interior of the channel, but excluding points nearest to the walls (see Fig. 1). We note that the spacing of candidate sensors can have influence on the resulting number of sensors and the performance of the controller that results from either sensor-selection approach. Neither the CE nor the BT approach is restricted to a particular candidate distribution. Chebyshev distributions are chosen out of simplicity in this study, since this matches the spatial discretization used in modeling the underlying fluid dynamics. Since the flow is spatially invariant, the sensor library is constructed based on Fourier coefficients. For streamwise disturbances, only wall-normal velocity information is relevant and so a sufficiently rich sensor library in this case is built-up using $\hat{\boldsymbol{v}}$ sensors only. For oblique and spanwise disturbances, we use $\hat{\boldsymbol{u}}$ and $\hat{\boldsymbol{v}}$ to build up our sensor library, so that $\text{rank}(C_n) = n$. We emphasize that these choices in the construction of the sensor library are not unique and are selected here mainly for simplicity.

In carrying out the CE approach (Algorithm 4), we begin by evaluating the L_2-norm for each column of the controller gain F_n, then rank these from largest to smallest (see Fig. 3). For each of the three wavenumber combinations reported in Fig. 3, there are a few columns with a relatively large L_2-norm compared to the others. Recall that a larger norm indicates that a sensor has a more dominant contribution to the control action, and so this indicates that the corresponding sensors should be retained, while sensors associated with smaller norms can be truncated. We do this in sequence, truncating all but the largest norm sensors, then re-designing the SOF-LQR controller. We compare the worst-case TEG for the new SOF-LQR controller with that of the full-information LQR. If the worst-case performance is not satisfactorily matched between the two, then we proceed to introduce the next set of dominant sensors according to the rankings in Fig. 3, and repeat this process until the resulting SOF-LQR controller recovers full-information LQR controller performance. Each graph of column norm versus number of sensors r_{CE} in Fig. 3 exhibits at least one "elbow point," and so we expect that we will be able to recover full-information LQR performance using a sparse sensor configuration with SOF-LQR control. Indeed, this will be the case. These results will be presented and discussed in more detail after we discuss the preliminary aspects of the BT procedure for sensor selection.

In conducting the BT approach for sensor selection, it is useful to evaluate system norms for the error dynamics associated with reduced-order balanced-truncation models as a function of model order r_{BT}. In the present study, the actuator dynamics are non-trivial—they are modeled with integral effect—and so the balancing transformation and associated model reduction procedure are specifically conducted only with respect to the input–output response of the fluid dynamic states $[\hat{\boldsymbol{v}}, \hat{\boldsymbol{\eta}}]^T$. Both the $\mathcal{H}_2$- and $\mathcal{H}_\infty$-norm of the error system are reported in Fig. 4, for each of the three disturbances considered. As expected, both system norms decrease with increasing model order. In fact, it is possible to find r_{BT} such that both system norms are less than a tolerance value err, where err is small. This indicates that the BT procedure will be able to identify a sparse sensor configuration for each disturbance by which SOF-LQR control will be able to recover full-information LQR control performance.

In the ensuing sections, we will analyze the sensor selection results from the CE and BT procedures more closely. We will do this for three types of disturbances: streamwise $(\alpha, \beta) = (1, 0)$, oblique $(\alpha, \beta) = (1, 1)$, and spanwise $(\alpha, \beta) = (0, 2)$. In each case, the worst-case (TEG maximizing) disturbance associated with the specific control law will be considered.

4.1 Streamwise disturbance $(\alpha, \beta) = (1, 0)$

The sensor configurations and the associated worst-case SOF-LQR control performance for streamwise disturbance with $(\alpha, \beta) = (1, 0)$ are presented in Fig. 5. The maximum TEG of the full-information LQR

[1] Note that what we refer to as "streamwise disturbances" in this study are spanwise constant in nature and exhibit waviness in the streamwise direction. Likewise, what we refer to as "spanwise disturbances" are streamwise constant and exhibit waviness in the spanwise direction.

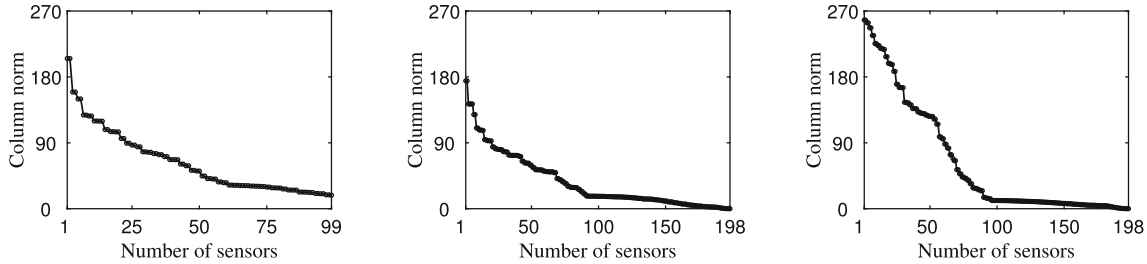

Fig. 3 In the gain column norm evaluation approach, evaluate the column norm of the gain matrix F_n. The L2-norms of each column are sorted in descend order

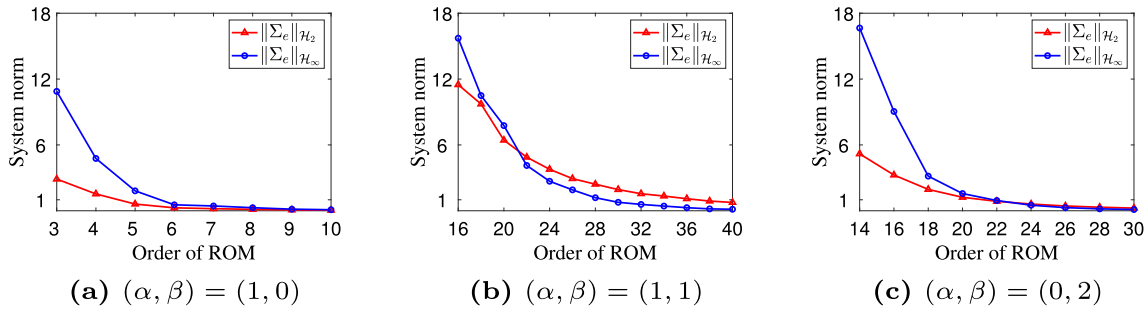

Fig. 4 In the balanced truncation approach, the error system norms are shown as a function of ROM order

controller (blue dotted line), the maximum TEG (G) for the SOF-LQR controlled flow are reported as a function of the number of sensors in Fig. 5a, with CE configurations denoted as red crosses and BT configurations as green dots. From this analysis, we see that SOF-LQR control recovers full-information LQR TEG performance when $r_{\text{BT}} \geq 6$ sensors are used based on the BT approach. Using the CE approach, SOF-LQR TEG performance recovers to within 5% of the full-information LQR TEG when $r_{\text{CE}} \geq 14$ sensors are used. In this case, the sufficiently rich library of candidate sensors C_n was constructed using only $\hat{\boldsymbol{v}}$ sensors. As such, the observed differences between the sensor configurations from BT and CE is purely due to the locations of these sensors. The specific sensor configurations obtained by the CE and BT sensor selection methods are illustrated in Fig. 5b, c respectively. By both approaches, the near-wall sensors are identified as important for the control starting with as few as $r_{\text{CE}} = r_{\text{BT}} = 3$ sensors. Except for the case with $r_{\text{CE}} = 9$, all the sensors selected by the CE approach are located either close-to-wall or clustered symmetrically about the channel centerline in the range $|y/h| = [0.77, 0.84]$. In contrast, the BT approach tends to yield asymmetrical arrangements in the channel and distributes sensors more uniformly between the channel walls. That said, BT does tend to place a higher concentration of sensors in a similar range as that of the CE from $|y/h| = [0.79, 1)$. As we will see, near-wall $\hat{\boldsymbol{v}}$ information also tends to be important for performance recovery due to oblique and spanwise disturbances as well.

We further investigate control performance for streamwise disturbances using the CE sensor configuration for $r_{\text{CE}} = 14$ and the BT sensor configuration for $r_{\text{BT}} = 6$. The sensor locations along with the optimal disturbance profiles for the SOF-LQR controllers leading from the CE and BT sensor arrangements are shown in Fig. 6. As can be seen here, the SOF-LQR controllers designed for sensor configurations from the CE and BT approaches yield similar optimal disturbance profiles as the full-information LQR controller. The sensors selected by the CE approach capture the near-wall spatial features of the $\hat{\boldsymbol{v}}$ disturbance profile. The BT approach yields sensors arrangements that tend to capture spatial features throughout the channel. Interestingly, the largest qualitative differences in the SOF-LQR optimal disturbance profiles arise in $\hat{\boldsymbol{u}}$, even though the sensor configurations are restricted to only $\hat{\boldsymbol{v}}$ sensors.

These differences—compared to the full-information case—are most visually prominent near the centerline for the BT configuration and near the walls for the CE configuration.

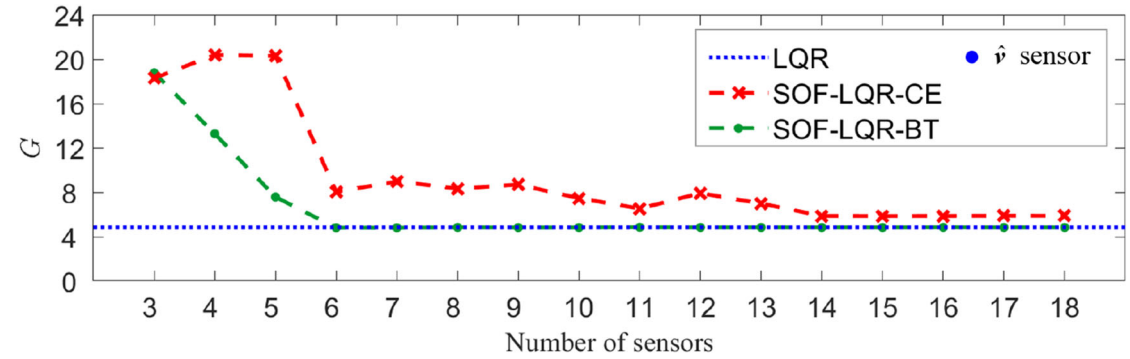

(a) Maximum TEG (G) versus number of sensors.

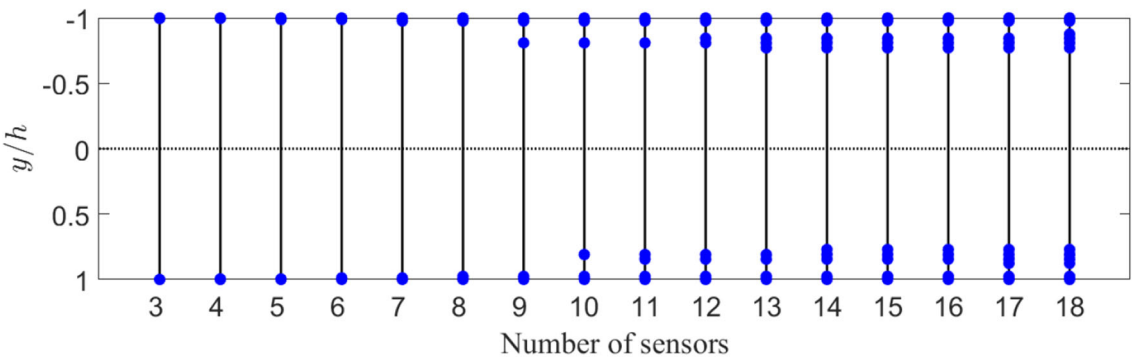

(b) Sensor locations from CE approach.

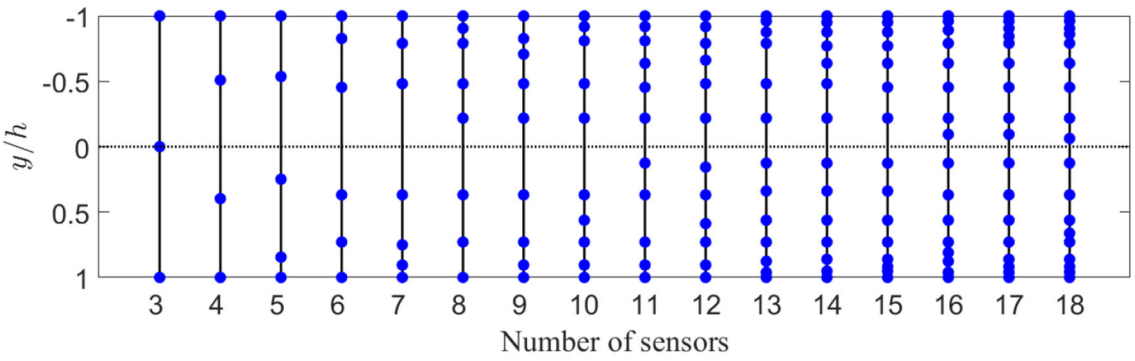

(c) Sensor locations from BT approach.

Fig. 5 Controller performance and sensor configurations for worst-case streamwise disturbances with $(\alpha, \beta) = (1, 0)$

4.2 Oblique disturbance $(\alpha, \beta) = (1, 1)$

Sensor configurations and the associated worst-case SOF-LQR control performance for oblique disturbances with $(\alpha, \beta) = (1, 1)$ are reported in Fig. 7. Figure 7a illustrates the maximum TEG (G) performance as a function of the number of sensors associated with the sensor configurations determined by CE (red cross) and BT (green dots) methods relative to the full-information LQR control performance (blue dotted line). The CE and BT approaches both recover full-information LQR performance when at least $r_{\mathrm{CE}} = 14$ and $r_{\mathrm{BT}} = 13$ total sensors are used, respectively. In Fig. 7b, c, the specific sensor configurations obtained by the CE and BT

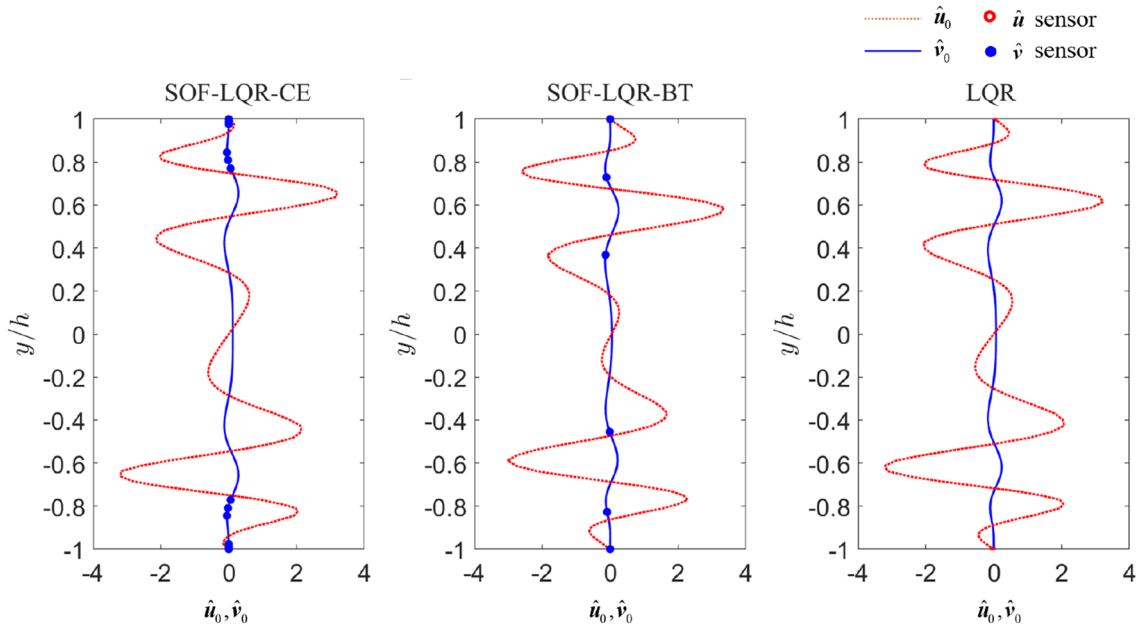

Fig. 6 The final selected sensor locations along with the optimal disturbance profile for wavenumber pair $(\alpha, \beta) = (1, 0)$. Sensor number $r_{CE} = 14$, $r_{BT} = 6$

sensor selection methods are reported. Note that both approaches were applied to the same candidate library of streamwise ($\hat{\boldsymbol{u}}$) and wall-normal ($\hat{\boldsymbol{v}}$) sensors. The BT method identifies both streamwise and wall-normal velocity sensors as important; whereas, the CE approach identifies that only wall-normal velocity sensors are important. In both approaches, the near-wall wall-normal velocity sensors are immediately identified as important for control, starting with $r_{CE} = r_{BT} = 2$ sensors. As the number of sensors is increased, the CE approach identifies wall-normal velocity sensors in the range $|y/h| = [0.48, 0.63]$ as important. In contrast, the BT approach does not select any $\hat{\boldsymbol{v}}$ sensors far from the walls until at least $r_{BT} \geq 11$ sensors are to be used. Instead, the BT approach tends to place $\hat{\boldsymbol{u}}$ sensors at or near the centerline of the channel. When $r_{BT} = 7$ or greater, SOF-LQR control based on the BT sensor arrangement yields TEG performance comparable to the full-information LQR controller. This appears to be due to the placement of $\hat{\boldsymbol{u}}$ sensors in the range $|y/h| = [0.5, 1)$. The CE approach requires more sensors for this performance recovery. For SOF-LQR controllers based on the CE approach, TEG performance is comparable to the full-information LQR control when $r_{CE} \geq 13$. As in the BT case, the CE approach finds that information in the approximate range $|y/h| = [0.5, 1)$ is important for recovering this performance, except now it is $\hat{\boldsymbol{v}}$ information that is deemed important.

We will investigate control performance for oblique disturbances in the remainder using the CE sensor configuration for $r_{CE} = 14$ and the BT sensor configuration for $r_{CE} = 13$. The optimal disturbance profile leading to the maximum TEG for controllers based on these CE and BT sensor arrangements are reported in Fig. 8. Similar to the streamwise disturbance case, the SOF-LQR optimal disturbance profiles from both the CE and BT sensor configurations are qualitatively similar to the full-information LQR optimal disturbance profiles. In both the CE and BT approaches, the placement of $\hat{\boldsymbol{v}}$ sensors indicates that near-wall wall-normal velocity information is important. In the CE case, the $\hat{\boldsymbol{v}}$ sensors capture the dominant spatial features of the $\hat{\boldsymbol{v}}$ disturbance profile. The distribution of $\hat{\boldsymbol{v}}$ sensors along the interior of the channel suggests that spatial derivatives $\hat{\boldsymbol{v}}$ are important. In contrast, the BT approach introduces only a single $\hat{\boldsymbol{v}}$ sensor away from the walls, which captures information near the spatial peak in the optimal wall-normal velocity disturbance profile. The BT approach emphasizes sensors that capture the prominent spatial features of the $\hat{\boldsymbol{u}}$ optimal disturbance profile.

4.3 Spanwise disturbance $(\alpha, \beta) = (0, 2)$

Sensor configurations and the associated worst-case SOF-LQR control performance for spanwise disturbances with $(\alpha, \beta) = (0, 2)$ are reported in Fig. 9. The maximum TEG (G) for the controlled flow is reported as a function of the number of sensors for sensor configurations determined by CE (red crosses) and BT (green

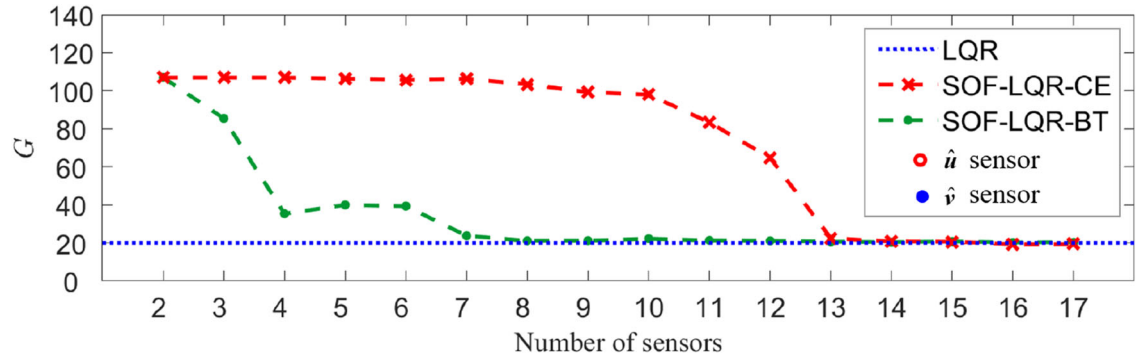

(a) Maximum TEG (G) versus number of sensors.

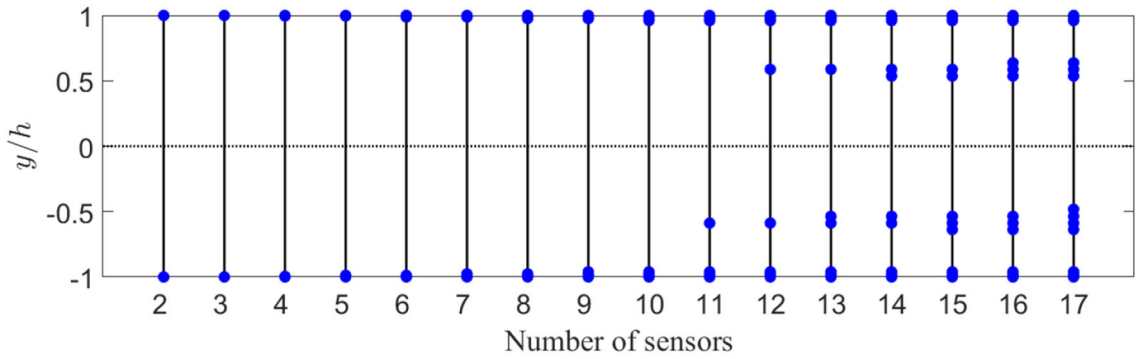

(b) Sensor locations from CE approach.

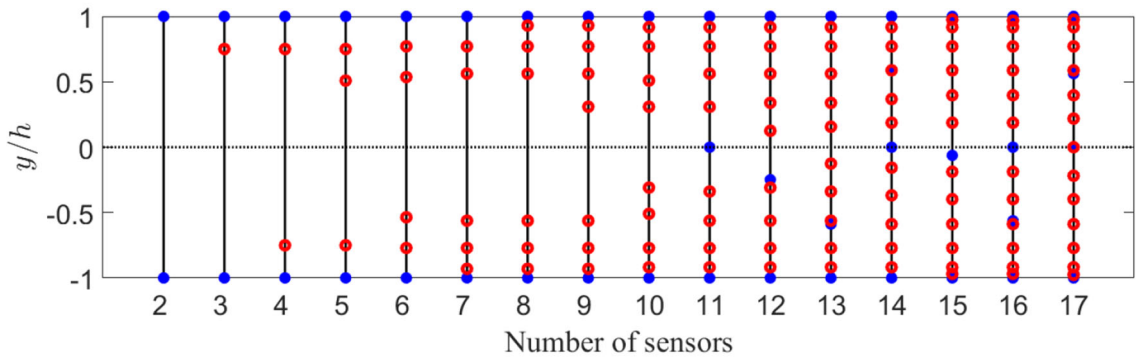

(c) Sensor locations from BT approach.

Fig. 7 Controller performance and sensor configurations for worst-case oblique disturbances with $(\alpha, \beta) = (1, 1)$

dots) methods in Fig. 9a. These are compared with the maximum TEG (G) for the full-information LQR controller (blue dotted line). From this analysis, it is evident that the BT approach yields a controller that recovers—at least approximately—the full-information control performance when $r_{\mathrm{BT}} \geq 10$. In contrast, the CE approach requires $r_{\mathrm{CE}} \approx 32$ sensors to get within 1% of the full-information TEG performance. Investigating the specific sensor configurations obtained by the CE and BT sensor selection methods—see figures 9b and 9c, respectively—provides some guidance on why this way be the case. The BT method identifies both streamwise and wall-normal velocity sensors as important, whereas the CE approach identifies that only wall-normal velocity sensors are important. Even more significant, the BT approach immediately

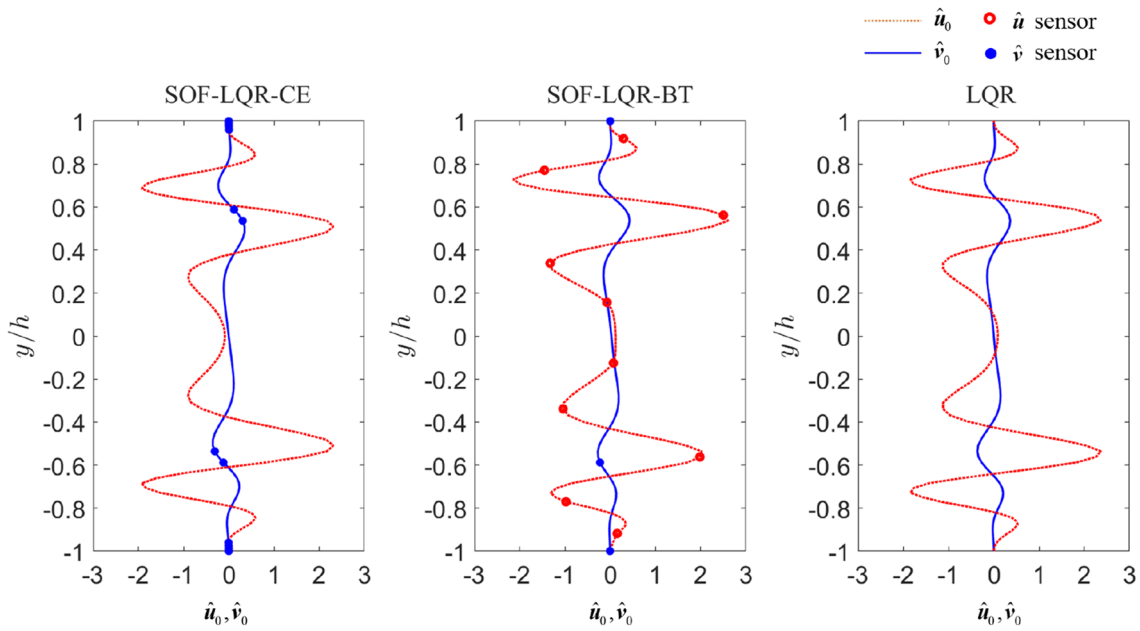

Fig. 8 The final selected sensor locations along with the optimal disturbance profile for wavenumber pair $(\alpha, \beta) = (1, 1)$. Sensor number $r_{\mathrm{CE}} = 14$, $r_{\mathrm{BT}} = 13$

($r_{\mathrm{BT}} = 2$) identifies that near-wall sensors are important for control. In contrast, CE does not identify this same near-wall information as important until $r_{\mathrm{CE}} \geq 32$. Up until $r_{\mathrm{CE}} = 32$, all of the sensors from the CE approach are clustered symmetrically about the channel center line in the range $| y/h | = [0.187, 0.588]$. The BT approach does not always yield asymmetric sensor arrangement, but the sensors are more evenly distributed throughout the interior of the channel. Given the TEG performance achieved with these sensor configurations, it is evident that wall-normal information in the vicinity of the walls and at the channel center line are important for TEG reduction for spanwise disturbances. Wall-normal velocity information at the center line is important, as the introduction of such a sensor allows the BT approach to recover full-information control performance with $r_{\mathrm{BT}} = 10$ sensors. In some of the BT arrangements, the center line $\hat{\boldsymbol{v}}$ sensor is replaced by or augmented with a $\hat{\boldsymbol{u}}$ sensor. In these cases, a pair of $\hat{\boldsymbol{v}}$ sensors tend to appear asymmetrically about the center line.

We note that the resulting asymmetric placement of sensors about the centerline in the BT approach is related to the numerical setup in the column-pivoted QR factorization. Specifically, in step 3 of Algorithm 2, the set of linearly independent rows in C_b—i.e., choice of sensors—is not unique, and the QR factorization yields one instantiation of a linearly independent set. Additionally, in this study, the candidate sensor library was constructed using velocity sensors located at Chebyshev points, which are especially dense in the vicinity of the channel walls. Thus, even though asymmetries arise in the resulting placement of sensors near the walls, this asymmetry tends to be within y/h=0.01 from an exactly symmetric placement. In cases where symmetry is required, we expect that this issue can be resolved by imposing constraints within the column-pivoted QR factorization and/or by ensuring that the candidate library includes sensors with adequate differences in type and location.

We will investigate control performance for spanwise disturbances in the remainder using the CE sensor configuration for $r_{\mathrm{CE}} = 32$ and the BT sensor configuration for $r_{\mathrm{BT}} = 16$. Note that the choice of $r_{\mathrm{BT}} = 16$ is motivated by the fact that the direct numerical simulations in section 5 run to completion more quickly for this case than for $r_{\mathrm{BT}} = 10$. The optimal disturbance profile leading to the maximum TEG for controllers based on these CE and BT sensor arrangements are reported in Fig. 10. Interestingly, the optimal disturbance profiles for the SOF-LQR controllers are strikingly similar to one another and to the optimal disturbance profile for the full-information LQR controller—even more so than in the previous cases considered for streamwise and oblique disturbances. In some sense, this is to be expected based on previously reported findings regarding the $(\alpha, \beta) = (0, 2)$ disturbance case. This wave-number pair exhibits the highest TEG among all wave-number pairs, and is the least affected by control [13–15]. In both the CE and BT approaches, we see that the $\hat{\boldsymbol{v}}$ sensors capture the dominant spatial features of the $\hat{\boldsymbol{v}}$ disturbance profile. However, only the BT sensor placements are able to capture the spatial profile associated with the $\hat{\boldsymbol{u}}$ component of the optimal disturbance. Although the

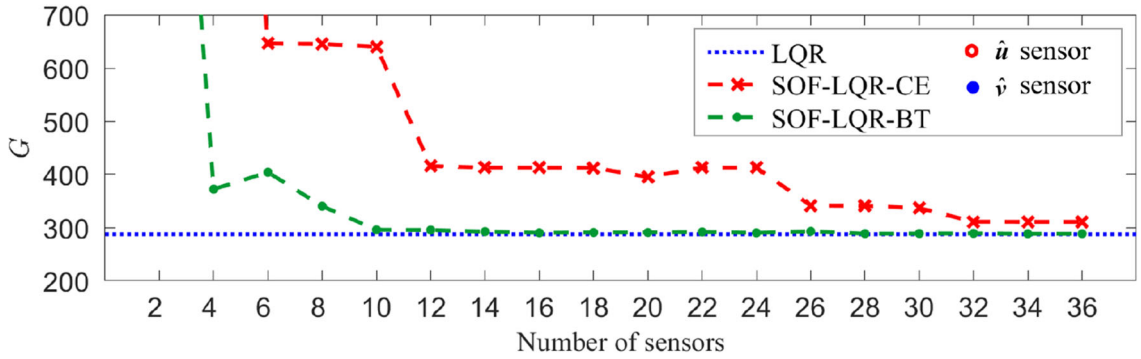

(a) Maximum TEG (G) versus number of sensors.

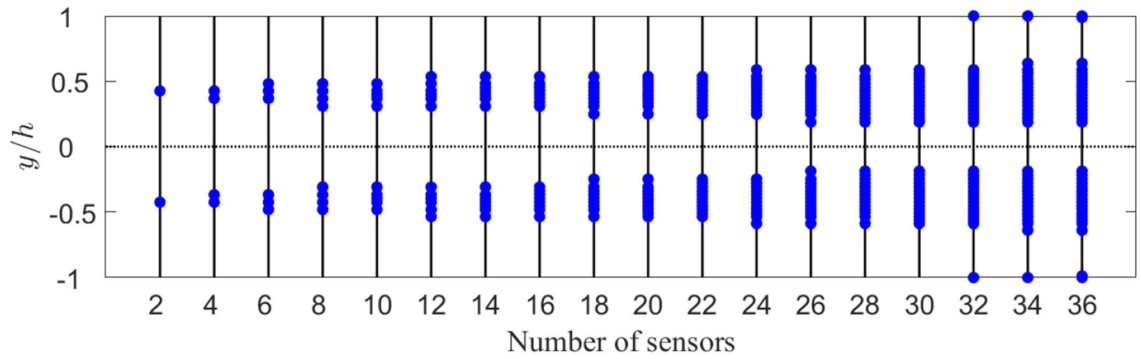

(b) Sensor locations from CE approach.

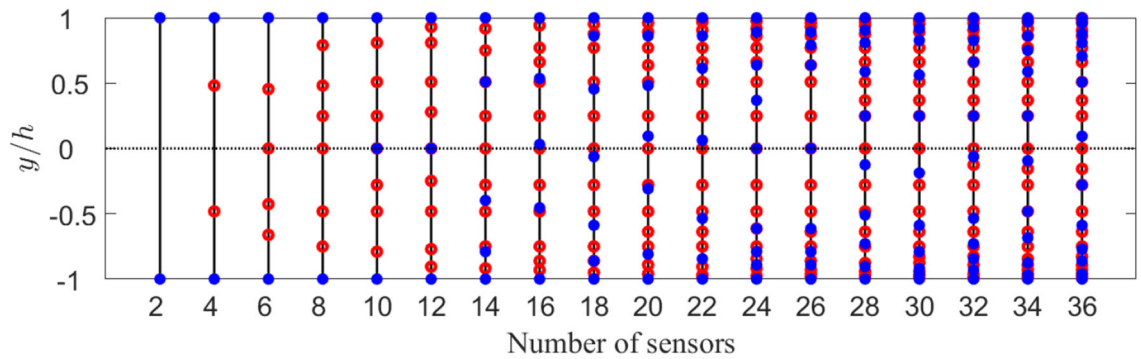

(c) Sensor locations from BT approach.

Fig. 9 Controller performance and sensor configurations for worst-case spanwise disturbances with $(\alpha, \beta) = (0, 2)$

$\hat{\boldsymbol{u}}$ component is smaller in magnitude compared with the $\hat{\boldsymbol{v}}$ component, this has an important consequence for TEG control performance.

Lastly, we considered configurations with only two to four sensors; however, SOF-LQR controllers designed with such sensor arrangements were unable to approximate—let alone recover—the full-information LQR control performance. Although these sparse sensor configurations did enable a modest reduction in TEG relative to the uncontrolled flow, their performance was nowhere comparable to the performance of SOF-LQR controllers designed with wall-based shear–stress and pressure sensing that we have considered in related work [24]. As such, those specific results are not reported here.

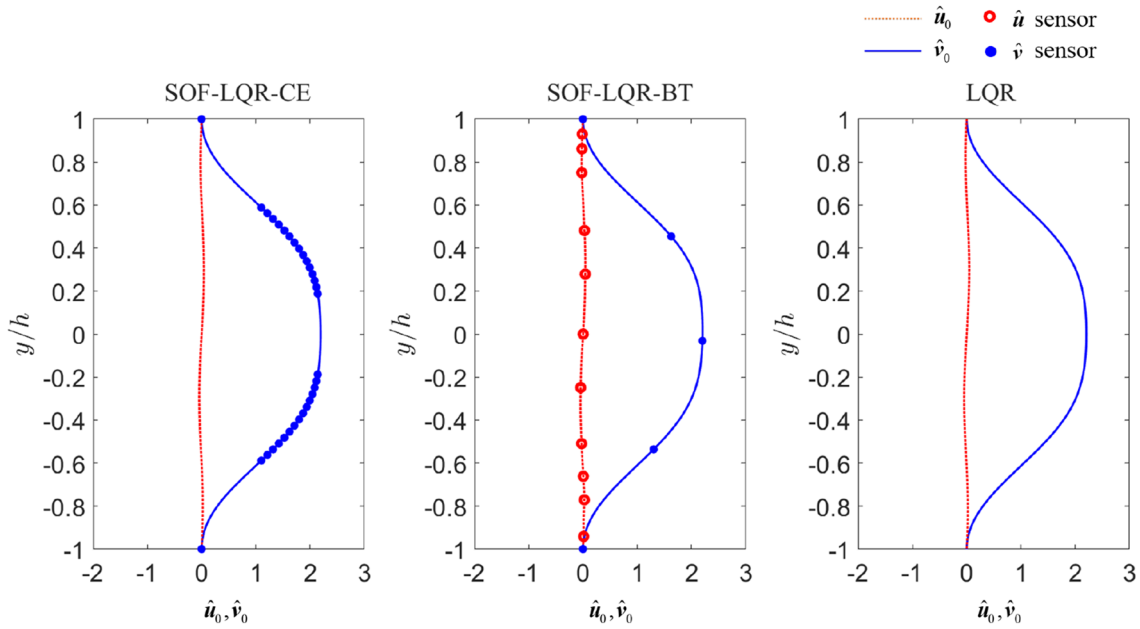

Fig. 10 The final selected sensor locations along with the optimal disturbance profile for wavenumber pair $(\alpha, \beta) = (0, 2)$. Sensor number $r_{CE} = 32$, $r_{BT} = 16$

Table 1 Sensor configurations used for detailed performance evaluation

(α, β)	Balanced truncation	Gain column norm evaluation
(1, 0)	0 u-sensors 6 v-sensors	0 u-sensors 14 v-sensors
(1, 1)	10 u-sensors 3 v-sensors	0 u-sensors 14 v-sensors
(0, 2)	11 u-sensors 5 v-sensors	0 u-sensors 32 v-sensors

4.4 Controller robustness analysis

Up to this point, all of the control performance analysis has been conducted for nominal conditions at $Re = 3000$. In this section, we will investigate the robustness of the TEG reduction when the controllers designed for $Re = 3000$ are applied at "off-design" subcritical Re values. The specific sensor arrangements we will investigate here correspond to the cases with a corresponding detailed analysis in the sections above. These are summarized in Table 1. The cost function J value for SOF-LQR with the selected sensors compared with LQR is reported in Table 2.

To investigate robust TEG performance, we again consider closed-loop system responses for optimal perturbations that result in the maximum TEG (G) for a given closed-loop system with control applied at the off-design Re. Results for SOF-LQR controllers designed at $Re = 3000$ then applied at $Re = [500, 5500]$ are reported in Fig. 11. The performance of both controllers at off-design Reynolds numbers is strikingly similar to the corresponding performance at on-design conditions at Reynolds numbers higher than 1000. These results demonstrate that SOF-LQR controllers can be designed based on BT and CE sensor arrangements *robustly* recover full-information LQR control performance; however, this robustness is not unconditional.

For streamwise wave disturbances at $Re \leq 500$, the SOF-LQR controllers designed for $Re = 3000$—using either CE or BT sensor arrangements—fail to reduce TEG relative to the uncontrolled flow. For spanwise wave disturbances at $Re \leq 1000$, the SOF-LQR designed for $Re = 3000$ based on the BT sensor arrangement lacks the same robust performance recovery characteristics as the CE sensor arrangement. In fact, the BT arrangement fails to reduce TEG relative to the uncontrolled flow at $Re \leq 500$. However, designs based on the CE sensor arrangement maintain the TEG reduction even at these lower Reynolds numbers. As the TEG under smaller Reynolds number is relatively low, it is not surprising that the TEG reduction ability also decreases.

Table 2 Cost function values for SOF-LQR with sensor configurations reported in Table 1 and full-information LQR

(α, β)	Balanced truncation	Gain column norm evaluation	LQR
(1,0)	6.85×10^3	7.86×10^3	6.78×10^3
(1,1)	3.72×10^4	3.90×10^4	3.63×10^4
(0,2)	7.82×10^6	7.91×10^6	7.82×10^6

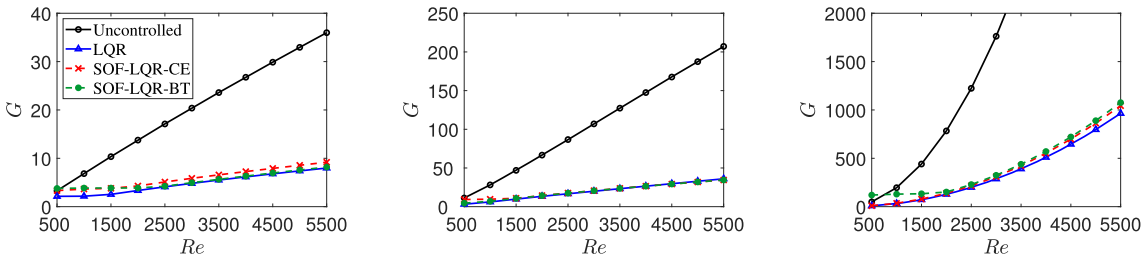

(a) $(\alpha, \beta) = (1, 0)$ $r_{CE} = 14$, $r_{BT} = 6$

(b) $(\alpha, \beta) = (1, 1)$ $r_{CE} = 14$, $r_{BT} = 13$

(c) $(\alpha, \beta) = (0, 2)$ $r_{CE} = 32$, $r_{BT} = 16$

Fig. 11 Robustness analysis

Though there are fewer chances that the transition will happen compared to higher Reynolds numbers, this suggests that we need to design the SOF-LQR controllers separately for TEG reduction at low Reynolds numbers. Indeed, SOF-LQR controllers designed using either BT and CE sensor arrangements at "on-design" conditions would recover the full-information LQR performance and reduce TEG relative to the uncontrolled flow.

Lastly, it is worth discussing controller robustness to wavenumber uncertainties, which can provide an indication of how the control will perform in response to disturbances of a broader nature. In related work [24], we have found that the full-information LQR controllers designed at a particular "on-design' wavenumber configuration exhibit robustness to variations in wavenumbers at "off-design" conditions. Owing to the ability of SOF-LQR controllers with BT and CE sensor arrangements to recover the closed-loop dynamics of the full-information LQR controller, these controllers are also expected to exhibit the same robustness properties. We further note that this robustness to wavenumber variations was also found to hold for SOF-LQR controllers designed with wall-based sensing strategies.

5 Results: nonlinear performance analysis using direct numerical simulations

Sensor selection for controller performance recovery was investigated using linear analysis in the previous section. Here, we are interested in determining the reliability of the resulting sensor-based output feedback control laws for transient energy growth reduction and transition control in the nonlinear setting. To this end, three-dimensional direct numerical simulations of plane Poiseuille flow at $Re = 3000$ are performed using a modified version of the spectral code *Channelflow* [45,46] to solve the incompressible Navier–Stokes equations. A second-order semi-implicit Crank-Nicolson Runge–Kutta temporal scheme is used. In past studies, the domain size is usually set to fit one wavelength of the wavenumber of interest for each direction. However, as the transition includes large-scale deformation of the original perturbation structures, the underlying physics during the transition processes cannot be fully captured with a limited domain size. Hence, we use a rectangular computational domain of size $8\pi h \times 2h \times 2\pi h$ in x-, y- and z-directions, respectively, which is relatively large in space to capture a broader extent of flow physics involved in the transition process. This provides a more realistic setting to assess transition control performance. To discretize the flow field, $N = 101$ Chebyshev points are specified in the y-direction, and 128×64 points are uniformly spaced along x- and z- directions, respectively. Periodic boundary conditions are assumed in the x- and z-directions in which the flow variables (velocity and pressure) are represented by Fourier expansion. No-slip boundary condition is specified at upper and lower walls for the uncontrolled flow. In the controlled flow, wall-normal velocity $\boldsymbol{v}(\pm h)$ is determined via feedback control law, while streamwise and spanwise velocities are zeros at the walls. Moreover, a constraint of

constant bulk velocity is specified. Grid resolution studies have been performed to ensure accuracy of results, as discussed in "Appendix C."

Actuation in the form of blowing and suction in y-direction is implemented on the entire upper and lower walls via temporally changing amplitude of wall-normal velocity $\boldsymbol{v}(\pm h)$. Because the control strategy is designed based on the linear dynamical system discussed above, both actuation and measurement are associated with the same wavenumber pair (α, β) as the optimal perturbation, but implemented within the nonlinear simulations; this allows flow control mechanisms to be isolated and investigated. In practice, a bank of linear controllers over all wave number combinations would be most effective. However, we note that the need for such a bank of controllers would have practical ramifications on the sensor configuration as well, since the set of sensors required for control at different wavenumber pairs within the bank would not necessary overlap. Nonetheless, it may be possible to achieve the desired performance with a small number of controllers in this bank: LQR and SOF-LQR controllers designed at certain wavenumbers exhibit robust TEG reduction at "off-design" wave numbers, as reported in [24]. This suggests that a single sensor configuration designed for each of the three disturbance types (streamwise, spanwise, and oblique disturbances) may be sufficient to achieve transition control; however, we do not investigate this possibility further in this study. In all cases, the value of wall-normal velocity on walls is determined by the feedback control law described in Sect. 3.

In the linear analysis of Sect. 4, characteristics of the optimal disturbance were examined solely using the linear dynamics. In the direct numerical simulations, baseline and controlled flows have an initial condition consisting of the base flow $[\bar{\boldsymbol{u}}, \bar{\boldsymbol{v}}, \bar{\boldsymbol{w}}] = [1 - (y/h)^2, 0, 0]$ and optimal disturbance $[\boldsymbol{u}_0', \boldsymbol{v}_0', \boldsymbol{w}_0']$ with a small amplitude. The kinetic energy density of the initial optimal disturbance is denoted by E_0. Moreover, a random perturbation is also introduced with kinetic energy density of 1% of E_0 into the flow to expedite an emergence of a laminar-to-turbulent transition in the flows, but has negligible influence on the feature of the optimal disturbance [47].

Simulations of 200 convective time units of the streamwise and oblique disturbance responses require approximately 200 CPU hours, regardless of whether or not the flow transitions to turbulence. The spanwise disturbance case is comparatively more computationally intensive, requiring approximately 1000 CPU hours to fully resolve the evolution of the flow from transient energy growth through a possible transition to turbulence. This difference is primarily driven by the fact that the transient energy growth mechanism in the spanwise disturbance response evolves on a longer time-scale than the associated responses to streamwise or oblique disturbances.

5.1 Laminar-to-turbulent transition

Direct numerical simulations are performed with various optimal disturbance amplitudes for each wavenumber pair. As shown in Fig. 12, the transient energy growth density for the smallest disturbance amplitude considered overlaps the linear result. Moreover, we find that the amplification of initial disturbance is suppressed as the amplitude of disturbance increases and nonlinear effects become prominent. Although smaller transient energy growth is observed in the cases with larger initial disturbances, the laminar-to-turbulent transition still emerges as indicated by dashed lines in Fig. 12. Indeed, large values of the absolute transient energy E, rather than the amplification E/E_0, is more likely to lead to transition. This also indicates that for the same initial disturbance, an ability to reduce the transient amplification can serve to suppress the laminar-to-turbulent transition.

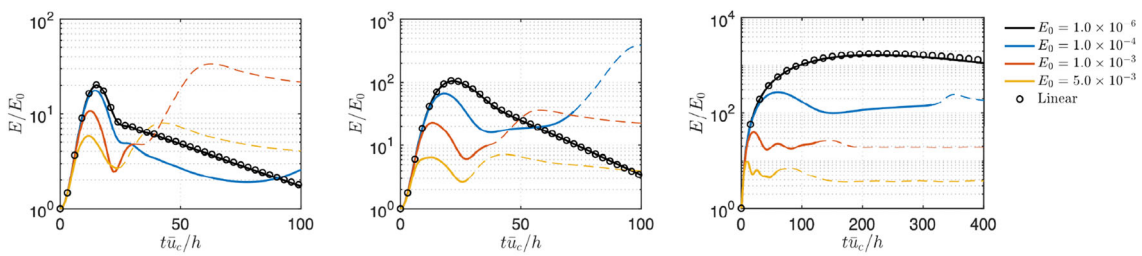

(a) $(\alpha, \beta) = (1, 0)$ **(b)** $(\alpha, \beta) = (1, 1)$ **(c)** $(\alpha, \beta) = (0, 2)$

Fig. 12 Transient energy growth of optimal disturbance with amplitude E_0. Dashed lines indicate that flow is turbulent state

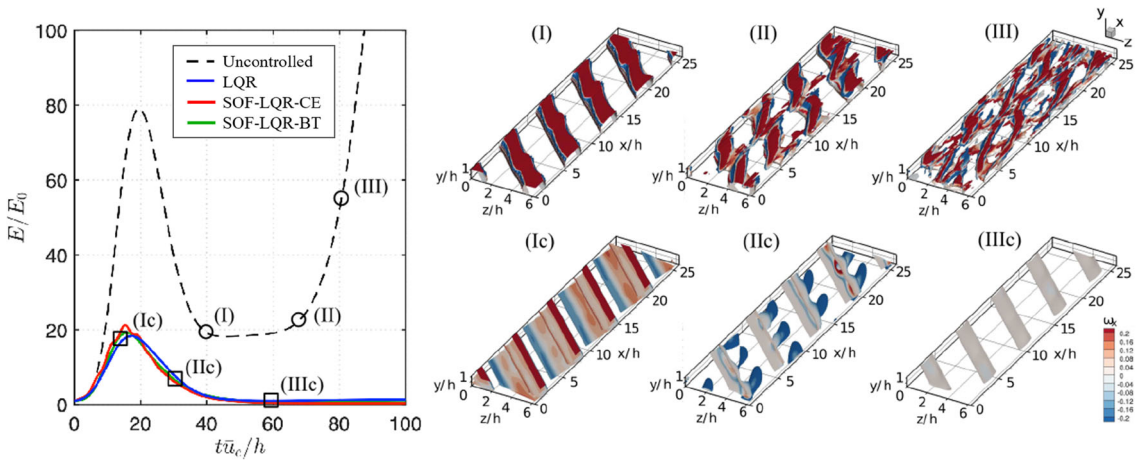

Fig. 13 In the oblique case, transient energy growth energy of uncontrolled flow and controlled flows ($E_0 = 5 \times 10^{-5}$) with controllers designed from LQR, balanced truncation, and gain column norm evaluation methods. Inserts are corresponding iso-surface of Q-criterion [48] colored by streamwise vorticity ω_x

5.2 Transition suppression

In the controlled flow, the sensor selection strategy evaluated in the direct numerical simulations is listed in Table 1. These strategies require the least number of sensors in output feedback control to recover the full-state LQR control performance in terms of reducing transient energy growth. For the streamwise disturbance with $(\alpha, \beta) = (1, 0)$, the threshold of minimal seed that leads to a laminar-to-turbulent transition increases from $E_0 = 1.0\times10^{-4}$ to $E_0 = 1.0\times10^{-3}$. For the oblique disturbance, the threshold increases from $E_0 = 5.0\times10^{-5}$ to $E_0 = 5.0 \times 10^{-4}$. However, for the spanwise disturbance, the controllers do not suppress transition, and actually lead to an earlier emergence of transition. This occurs for the full-information controller as well [14]. Although TEG performance is recovered, this case shows that TEG reduction is not the only objective to be considered when it comes to transition control.

5.2.1 Oblique and streamwise disturbances

Because the transition and control mechanisms in oblique $(\alpha, \beta) = (1, 1)$ and streamwise $(\alpha, \beta) = (1, 0)$ disturbances are similar, we will mainly use oblique case as an example to discuss how the controller modifies the flow and ultimately suppresses laminar-to-turbulent transition.

In the case of oblique disturbance with optimal disturbance amplitude of $E_0 = 5 \times 10^{-5}$, the transient energy growth density reaches maximum amplification of $E/E_0 \approx 80$ at $t\bar{\boldsymbol{u}}_c/h = 20$ as shown in Fig. 13. Representative flowfields at different stages are displayed to illustrate the transition mechanism. Before stage (I), oblique coherent structures develop from small to large scale as transient energy grows. At stage (I), although the transient increase of perturbation kinetic energy has decreased to a relatively lower value, a large value of streamwise vorticity is observed along the oblique coherent structures near the wall. At stage (II), streamwise vortical structures start to grow stemming from the oblique coherent structures. As these structures develop, they interact with each other and break down into small scale structures. From this, a laminar-to-turbulent transition emerges at stage (III). In all the three controlled flows, the maximum transient energy growth densities are reduced to $E/E_0 \approx 20$ around $t\bar{\boldsymbol{u}}_c/h = 18$, and their trajectories are similar. The control mechanism is similar among the SOF-LQR controllers based on BT and CE sensor configurations and the full-information LQR controller. Here we use snapshots of flow fields with the SOF-LQR controller designed using the sensor configuration from the BT method as an example in Fig. 13. At stage (Ic) in the controlled flow, the coherent structures remain almost uniform in the oblique direction, with smaller values of streamwise vorticity generated near the walls. As transient energy decreases at stage (IIc), the only oblique structures observed in Fig. 13 are induced from the wall actuation. As time further elapses, the streamwise vortical structures decay and actuation amplitude also decreases, ultimately suppressing the transition observed in the uncontrolled flow.

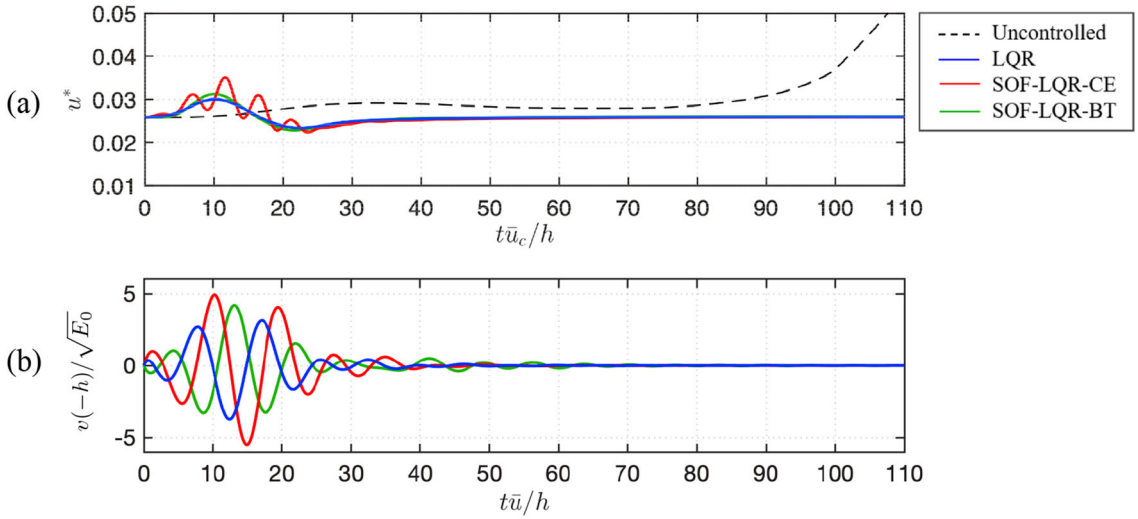

Fig. 14 **a** Friction velocity and **b** Fourier coefficient of wall-normal velocity boundary condition $v(-h)$ at lower wall of flow ($E_0 = 5 \times 10^{-5}$) with $(\alpha, \beta) = (1, 1)$

Friction velocity has been used as a quantity to identify the laminar-to-turbulent transition in the flow, which is defined as

$$u^* = \sqrt{\frac{\tau_w}{\rho}}, \tag{22}$$

where $\tau_w = \mu(\partial u/\partial y)$, μ is dynamic viscosity, and the density ρ is set to one for the incompressible flow. The friction velocity at the lower wall is calculated using mean flow quantity. The time-history of the friction velocity for uncontrolled and controlled flows are shown in Fig. 14. A sudden increase in friction velocity in the uncontrolled flow (see Fig. 14a) indicates an emergence of the transition. In the controlled flows, the actuation is turned on to introduce blowing and suction during the transient energy growth period (see Fig. 14). Correspondingly, we also observed that the friction velocity varies as the actuation is active. As the kinetic energy grows, the friction velocity increases. When the kinetic energy decreases, the friction velocity reduces to a lower value and then stays at a constant value. Particularly, the friction velocity with the controller designed using the CE sensor configuration has a high-frequency oscillation during the transient process, but the general trend is similar to the other two controlled cases.

Slices of uncontrolled and controlled flowfields are displayed in Fig. 15 to show modifications of the flow features due to wall actuation. The slices are extracted at convective time of $t\bar{\boldsymbol{u}}_c/h = 18$, when the kinetic energy density reaches its maximum value. In the uncontrolled flow, large wall-normal velocity fluctuations reside in the center between the upper and lower walls. The size of the coherent structures highlighted by Q-criterion is about half height of the channel as the transient energy grows. From the flowfields shown in Fig. 13 and our previous study [14], the existence of these large coherent structures induces a large value of streamwise vorticity and generates streamwise vortical structures. Once these vortical structures break down, a transition to turbulence emerges. In all the three controlled flows, we observed that the wall-normal velocity actuation modifies the pattern of velocity flowfields and changes the distribution of high-shear regions. This change of flow hinders the formation of large coherent structure, which in turn prevents laminar-to-turbulent transition from arising in the flow.

5.2.2 Spanwise disturbance

In the cases with spanwise $(\alpha, \beta) = (0, 2)$ optimal disturbance considered in the present work, none of the controllers increase the threshold of laminar-to-turbulent transition. In fact, the controllers actually worsen the transition scenario. As shown in Fig. 16a of case with $E_0 = 5 \times 10^{-5}$, there is no laminar-to-turbulent transition in the uncontrolled flow, but the controllers trigger the transition. While the controller is active, actuation amount in the form of blowing and suction gradually decreases as shown in Fig. 16b. As being closely examined in our previous study [14], the control input introduces streamwise vortices near walls,

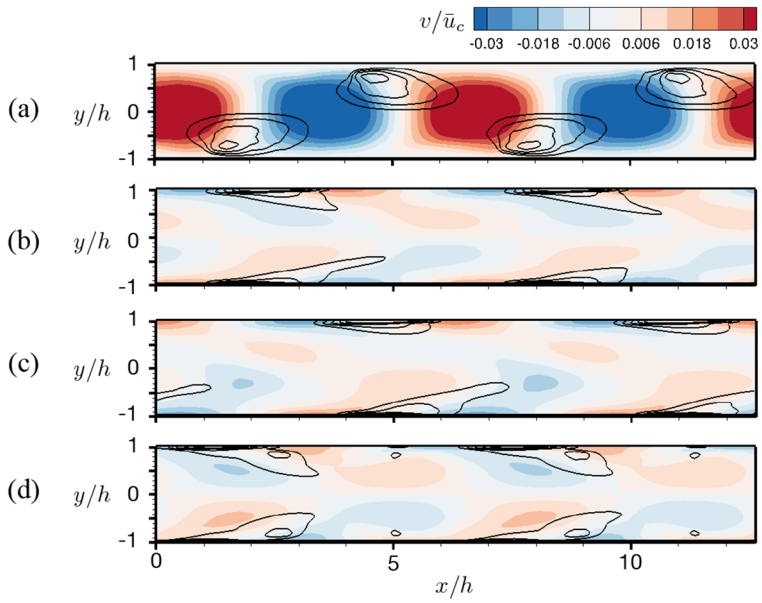

Fig. 15 Contours of wall-normal velocity and Q-criterion over a range of $[0.01, 0.05]$ at slice of $z/h = 0$ of flow ($E_0 = 5 \times 10^{-5}$) with $(\alpha, \beta) = (1, 1)$ at $t\bar{u}_c/h = 18$ **a** Uncontrolled flow, and controlled flow with controller designed by **b** LQR, **c** balanced truncation, and **d** gain column norm evaluation methods

which hinder the merging process of vortex pairs in the center of the channel, resulting in a reduction of transient energy growth. However, the control input creates high-shear regions near the wall where secondary instabilities creep in and cause a laminar-to-turbulent transition. This phenomenon suggests that decreasing transient energy growth from linear analysis is not sufficient to suppress (or even delay) the transition. This early onset of transition in nonlinear simulations can be alleviated by increasing the control penalty in the LQR objective function [24]. Sensor-selection using this improved baseline full-information control law would also result in improved performance for the SOF-LQR controllers.

Interestingly, using the same objective function, but limiting the information available for static output feedback control to wall shear stress measurements only, actually enables transition suppression in this case, and transition delay for large amplitude disturbances [24] as shown in Fig. 17a. During the time period considered in the present study, the SOF-LQR controller does not worsen the transition and leads to a lower friction velocity compared to uncontrolled flow. As seen in Fig. 17b, the normalized actuation velocity is smaller than the one shown in Fig. 16. Correspondingly, the reduction of transient energy growth with SOF-LQR control with only shear stress measurements is roughly 40% of the reduction achieved by full-information LQR with respect to maximum transient energy growth (see Fig. 17c). This SOF-LQR with shear–stress sensors at the walls is able to modify the flow sufficiently to delay transition and does so with a gentle actuation such that the control does not trigger other instabilities in the nonlinear flow that cause a transition.

6 Discussion and conclusions

In this paper, we proposed and investigated two approaches for sensor selection to enable sensor-based output feedback controllers to recover full-information performance. Both approaches leveraged the fact that, with a sufficiently rich set of sensors, a static output feedback (SOF) controller can always be designed to recover full-information control performance exactly. Thus, we showed that the problem of sensor selection for performance recovery could be recast as a problem of sensor down-selection from a sufficiently rich library of candidate sensors. One approach for sensor selection was based on a column-norm evaluation (CE) of the SOF controller gain matrix used to achieve full-information performance; the other approach was based on a balanced truncation (BT) procedure for model order reduction of linear dynamic systems.

Both sensor-selection methods were demonstrated on the problem of transient energy growth (TEG) reduction and transition suppression in a channel flow at the sub-critical Reynolds number of $Re = 3000$ using linear quadratic optimal control strategies. All sensor-based output feedback controllers in this study were designed

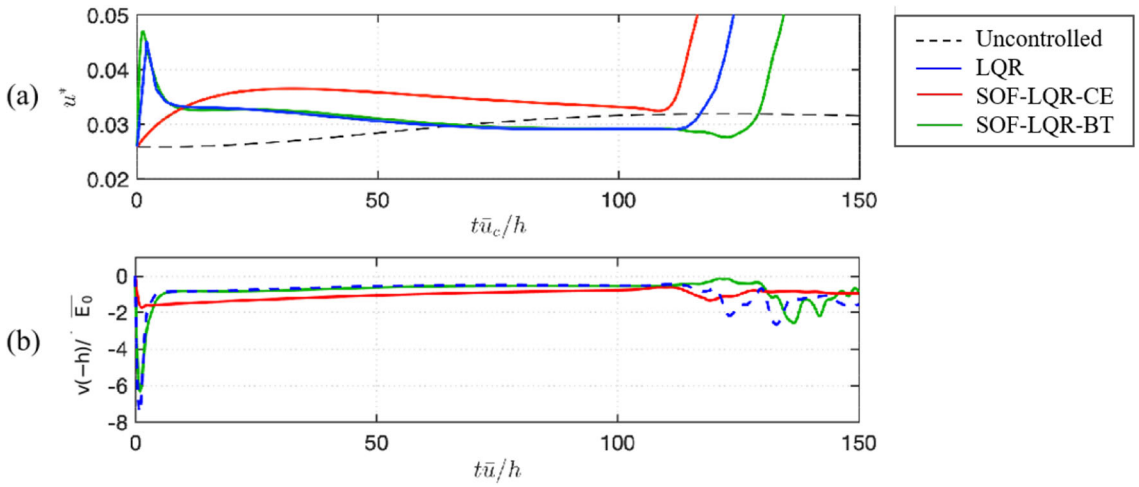

Fig. 16 **a** Friction velocity and **b** Fourier coefficient of wall-normal velocity boundary condition $v(-h)$ at lower wall of flow ($E_0 = 5 \times 10^{-5}$) with $(\alpha, \beta) = (0, 2)$

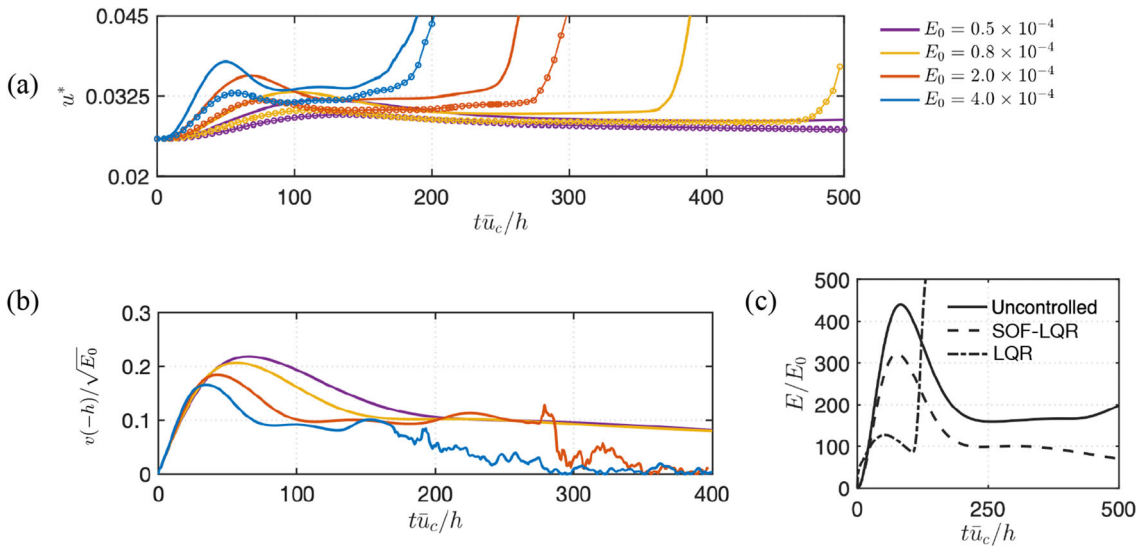

Fig. 17 With only shear–stress sensors at the walls, **a** friction velocity of uncontrolled and controlled cases. Solid line with circles represents controlled case. **b** Fourier coefficient of wall-normal velocity boundary condition $v(-h)$ in controlled flows. **c** Transient energy growth of uncontrolled and controlled flow with disturbance amplitude of $E_0 = 5 \times 10^{-5}$

based on SOF-LQR synthesis and compared with full-information LQR controllers designed based on the same quadratic control objective. Based on linear performance analyses, both the CE and BT sensor selection approaches identified sensor configurations that enabled SOF-LQR control to recover full-information LQR control performance for optimal streamwise, oblique, and spanwise disturbances. In all cases where performance recovery was achieved, the optimal disturbance profiles for the SOF-LQR controlled flows were qualitatively similar to those for the full-information LQR controlled flows. These similarities were most striking in the case of spanwise disturbances, but all corroborate the fact that the dynamic responses of all of these controlled systems are approximately the same. Sensors selected by the BT and CE approaches tended to be placed in the vicinity of prominent spatial features associated with these optimal disturbance profiles. Further, we found that SOF-LQR controllers designed based on these sensor configurations also exhibited robustness to variations in the Reynolds number. Controllers designed for $Re = 3000$ continued to achieve comparable worst-case TEG performance to the full-information LQR controller when applied over a range of "off-design" sub-critical Reynolds numbers.

In general, the BT approach required fewer sensors to recover full-information control performance compared to the CE approach. Wall-normal velocity information near the channel walls was consistently determined to be important for control performance by both methods over all disturbances considered. However, the arrangement and type of other sensors between the CE and BT approaches differed otherwise. Our results for the oblique and spanwise disturbance designs suggest that TEG control benefits from streamwise velocity information—more so than wall-normal velocity information—along the channel interior. For these cases, both streamwise and wall-normal velocity sensors were available in the candidate sensor library. Yet, the CE approach consistently removed streamwise velocity sensors in favor of wall-normal velocity sensors, which may contribute to the need for more sensors for performance recovery relative to the BT approach. The BT approach consistently yielded a heterogeneous set of sensors, with wall-normal velocity sensors near the walls and streamwise velocity sensors along the channel interior.

In addition to the linear analysis, we conducted direct numerical simulations (DNS) to evaluate control performance in the nonlinear setting. SOF-LQR controllers designed based on both sensor selection approaches continued to recover full-information controller performance in DNS. For streamwise and oblique disturbances, the SOF-LQR controllers successfully increased the disturbance energy threshold for transition by an order of magnitude. We found that control hindered the formation of large coherent structures, in part because actuation from the wall served to modify the shear distribution in the flow. With a reduced size of coherent structures, the amount of induced streamwise vortical streaks decreased and ultimately suppressed the transition that was observed in the uncontrolled flow. We also note that TEG reduction observed in linear analysis was not sufficient for preventing transition in the nonlinear simulations. The linear analysis missed the secondary instabilities that were excited by actuation in the case of spanwise disturbances. These nonlinear interactions promoted an earlier transition, even though the TEG was reduced. Controller designs that explicitly account for these nonlinear interactions should be investigated in future studies.

Finally, we note that the sensor selection methods presented here are more generally applicable to other performance objectives, sensor-types, and flow configurations. So long as an acceptable full-information controller is available and a sufficiently rich sensor library can be constructed to adhere to any spatial/physical constraints, then both the CE and BT approaches can be used to downselect to a sparse set of sensors. Neither sensor-selection approach has limitations with respect to the candidate set of sensors or their locations; however, there is no guarantee that the number of sensors required to recover full-state feedback performance will be a small fraction of the original candidate set, even though such a reduction was possible in this study. In addition, the sensor selection methods proposed here can provide insights into the most important sensors for closed-loop performance. This creates opportunities to guide the choice of sensors in the numerous applications where a complete recovery of full-information control performance is not required.

In addition, both the CE and BT approaches introduced for sensor selection in this study can be trivially extended to the problem of actuator selection, simply by considering the dual problem and a sufficiently rich library of candidate actuators. We hope that the promising results demonstrated in this paper will lead to further adoption and refinement of these strategies into the future.

Acknowledgements This material is based upon work supported by the Air Force Office of Scientific Research under award number FA9550-19-1-0034, monitored by Dr. Gregg Abate, and the National Science Foundation under award number CBET-1943988, monitored by Dr. Ronald D. Joslin.

Declarations

Conflict of interest The authors report no conflict of interest.

Appendix A Anderson-Moore algorithm with Armijo-type adaptation

Algorithm 3 presents the Anderson-Moore algorithm with Armijo-type adaptation that can be used to solve an SOF-LQR controller [16,24]. The SOF-LQR problem consists of a coupled set of nonlinear matrix equations whose solution may not yield a global optimal solution. The Anderson-Moore algorithm is an iterative method for computing a locally optimal solution. The algorithm requires an initial stabilizing SOF control, which can influence the resulting SOF-LQR controller. In this work, Algorithm 3 is initialized using a SOF control gain determined using an iterative linear matrix inequality approach [21,24]. Subsequently, the complexity of a single iteration of the Anderson-Moore algorithm with Armijo type adaptations is of $\mathcal{O}(n^3)$. Additional details regarding the SOF-LQR synthesis methods used here can be found in [24].

Algorithm 3: ***Anderson-Moore algorithm with Armijo-type adaptation***

step 0: Set $i = 0$, initialize $F_i = F_0$ to be any $F_0 \in D_s$, where D_s is the set of all stabilizing SOF controllers. Set $0 < \xi < 1$, $0 < \sigma < 1/2$, and $\delta > 0$.
step 1: Solve $S(F_i)$ in

$$S(F_i)[A + BF_iC] + [A + BF_iC]^{\mathsf{T}} S(F_i) + C^{\mathsf{T}} F_i^{\mathsf{T}} RF_iC + Q = 0.$$

step 2: Set $X_E = \mathrm{E}\{X(0)X(0)^{\mathsf{T}}\}$, solve $H(F_i)$ in

$$H(F_i)[A + BF_iC]^{\mathsf{T}} + [A + BF_iC]H(F_i) + X_E = 0.$$

step 3: Find the smallest integer $\gamma_1 \geq 1$ such that $F_i + \xi^{\gamma_1}\mathrm{T}_i \in D_s$, where

$$\mathrm{T}_i = -F_i - R^{-1}[B^{\mathsf{T}} S(F_i)H(F_i)C^{\mathsf{T}}][CH(F_i)C^{\mathsf{T}}]^{-1}.$$

step 4: Find the smallest integer $\gamma_M \geq \gamma_1$ such that

$$J(F_i + \xi^{\gamma_M}\mathrm{T}_i) \leq J(F_i) + \sigma\xi^{\gamma_M}\mathrm{trace}(\frac{\partial J}{\partial F_i}^{\mathsf{T}}\mathrm{T}_i).$$

step 5: Find integer $\ell \in \{\gamma_1, \ldots, \gamma_M\}$ such that

$$J(F_i + \xi^{\ell}\mathrm{T}_i) = \min J(F_i + \xi^{j}\mathrm{T}_i), \text{ where } j \in \{\gamma_1, \cdots, \gamma_M\}.$$

step 6: Set $F_{i+1} = F_i + \xi^{\ell}\mathrm{T}_i$, $i = i + 1$.
step 7: Check $\|\frac{\partial J}{\partial F_i}\|_2 \leq \delta$. If true, stop. Otherwise, go to **step 1**.

Appendix B A comparison of column-norm evaluation with convex-optimization-based sparse control synthesis

The column-norm evaluation (CE) method proposed in Sect. 3.1 is a simple heuristic that facilitates sensor selection for large-scale problems. The CE heuristic was inspired by the convex-optimization-based methods proposed in [41]. Here we will provide justification for the CE method by comparing with a convex-optimization-based design on a system for which convex synthesis is computationally tractable. Although the CE method is still heuristic in nature, this example will establish that it is at least a reasonable heuristic to consider when computationally intensive convex-optimization-based methods are not tractable.

Consider the linear state-space system,

$$\dot{x} = Ax + Bu \tag{B1}$$
$$y = Cx, \tag{B2}$$

where

$$A = \begin{bmatrix} -0.0046 & -0.1978 & 0.0039 & 0.0133 & 0.0127 & -0.0285 & 0 & 0 \\ 0.0380 & -0.5667 & -0.0029 & -0.0014 & -0.0100 & -0.0232 & 0 & 0 \\ 0.3259 & 0.3570 & -0.2947 & -0.4076 & -0.8152 & 0.1064 & 1.0000 & 0 \\ -0.0045 & -0.0378 & 0.0070 & -0.0654 & -0.0397 & 0.0709 & 0 & 0 \\ -0.4020 & -0.2149 & 0.2266 & -0.4093 & -0.8210 & -0.2786 & 0 & 1.0000 \\ -0.0730 & 0.5683 & 0.0148 & 0.2674 & 0.1442 & -0.7396 & 0 & 0 \\ -9.8100 & 0 & 0 & 0 & 0 & 0 & 0 & 0 \\ 0 & 0 & 0 & 9.8100 & 0 & 0 & 0 & 0 \end{bmatrix},$$

$$B = I_{8\times 8},$$

$$C = \begin{bmatrix} 0.0676 & -1.1151 & 0.0062 & -0.0170 & -0.0129 & 0.1390 & 0 & 0 \\ 0.1221 & 0.1055 & -0.0682 & 0.0049 & 0.0106 & 0.0059 & 0 & 0 \\ -0.0001 & 0.0039 & 0.0010 & 0.1067 & 0.2227 & 0.0326 & 0 & 0 \\ -0.0016 & 0.0035 & -0.0035 & 0.1692 & 0.1430 & -0.4070 & 0 & 0 \end{bmatrix}.$$

Table 3 Column norm values of the SOF gain matrix F

Column 1	Column 2	Column 3	Column 4
1.8853	21.1077	11.9121	6.6448

The dual of this system was used to demonstrate row-sparse controller synthesis in [41] and was reported as benchmark problem HE3 [49] corresponding to a linearized 8-state model of the Bell 201A-1 Helicopter. We work with this modified version of the problem here so as to study column-sparse controller synthesis, corresponding to sensor selection and the CE method.

Our first step will be to compute an optimal controller according to [41]. Since $B = I$, this turns out to be a convex problem that can be solved via (B3) in the sparse LQR step of Algorithm B, to be described momentarily. The initial condition is set to $x_0 = [1, 1, ..., 1]^T$, following the choice in [41]. Solving for the exact optimal control gain F^{exact}, we obtain

$$F^{\text{exact}} = \begin{bmatrix} -0.0181 & -0.9803 & 0.1325 & 0.0028 \\ 0.7672 & -0.1281 & -0.0674 & 0.0205 \\ -1.8853 & 19.6594 & -0.6169 & 1.5326 \\ 0.0896 & -0.1614 & -0.7120 & -0.4899 \\ 0.2274 & -0.1401 & -6.6221 & -3.0483 \\ 0.0154 & 0.0517 & -0.8353 & 0.1169 \\ -1.4943 & 21.1077 & -4.2401 & 0.0429 \\ 0.9987 & -4.3681 & -11.9121 & -6.6448 \end{bmatrix}.$$

The optimal cost associated with this solution is $J^{\text{exact}} = 1.32 \times 10^3$.

In order to apply the CE heuristic, we evaluate the column norms of the gain matrix F^{exact} (see Table 3). According to the CE heuristic, the first column of F^{exact} (i.e., the sensor associated with the first row of C) is least important to the closed-loop performance, and so can be removed. By the CE approach, the next candidate for removal would be the second column of F^{exact}, or the second row of C. Finally, the last candidate for removal would be column 3 of F^{exact}, or the sensor associated with the third row of C. In our example, we opt to remove two sensors. Following the CE sequence identified above, we have

$$C^{\text{CE}} = \begin{bmatrix} 0.1221 & 0.1055 & -0.0682 & 0.0049 & 0.0106 & 0.0059 & 0 & 0 \\ -0.0001 & 0.0039 & 0.0010 & 0.1067 & 0.2227 & 0.0326 & 0 & 0 \end{bmatrix}.$$

We now re-solve for the optimal control via (B3), which yields

$$F^{\text{CE}} = \begin{bmatrix} -0.9823 & 0.1772 \\ -0.0393 & 0.0313 \\ 19.8284 & -0.3111 \\ -0.1582 & -0.7959 \\ -0.2287 & -7.7153 \\ 0.1156 & -0.8048 \\ 21.3852 & -4.6557 \\ -4.5979 & -13.9553 \end{bmatrix}.$$

The cost associated with this solution will be $J^{\text{CE}} = 1.39 \times 10^3 \approx 1.05 J^{\text{exact}}$. Note that to achieve a sparse sensor solution, a small (5%) price was paid on the performance.

Now to compare with a more rigorous (i.e., non-heuristic) solution approach to establish some justification for the CE heuristic. A column-sparse controller can be obtained by working with Algorithm 4, listed at the end of this appendix. This is a convex-optimization-based controller synthesis that seeks a column-sparse design. The row-sparse control synthesis version of this algorithm was proposed in [41]. The basic idea is to relax the original objective function J to allow for some sparsity in the resulting control design. This is reflected in the condition (B4), where ξ is a user-selected design parameter. A larger ξ will allow for a sparser controller, while $\xi \to 1$ will tend toward the original optimal control solution. For additional details on the derivation of this algorithm, we refer the reader to [41].

In applying Algorithm 4, we set $\xi = 1.25$ in (B4). This was the same value used in the example reported in [41]. In step 3, we use 10^{-8} for the zeroing threshold. The resulting controller gain is

$$F^{\text{convex}} = \begin{bmatrix} 0 & -0.9662 & 0.1954 & 0 \\ 0 & -0.0314 & 0.0404 & 0 \\ 0 & 19.5898 & -0.5827 & 0 \\ 0 & -0.1424 & -0.7770 & 0 \\ 0 & -0.1352 & -7.6064 & 0 \\ 0 & 0.1383 & -0.7835 & 0 \\ 0 & 21.2576 & -4.8017 & 0 \\ 0 & -4.3871 & -13.7127 & 0 \end{bmatrix}.$$

The associated cost of this column sparse controller is $J^{\text{convex}} = 1.39 \times 10^3 \approx 1.05 J^{\text{exact}}$.

Two observations regarding these solutions provide justification for the CE method: (1) the same set of sensors is removed/retained between the CE method and the convex-optimization-based synthesis, and (2) the associated cost function for both the CE and convex-optimization-based methods are comparable ($1.05 J^{\text{exact}}$). We note that the specific gain values are different between the two methods. This is an artifact of the manner in which the gains were computed. In the convex-optimization-based control synthesis, the zero rows in the C matrix were not removed, whereas in the CE method they were handling the C matrix in the same manner.

Since the same sparse sensor solution is obtained, a re-design of F^{convex} with those zero rows removed does yield an identical control solution F^{CE} as obtained by the CE method. The converse is also true. We note that the correspondence between the CE method and the convex-optimization-based method is dependent on the user-specified design variable ξ. As such, this correspondence between solutions is not guaranteed. Nonetheless, as we saw in this example, it is possible for the CE method to achieve a comparable solution as the convex-optimization-based approach for particular values of the design parameter ξ.

While we have established some justification for the CE method, this justification is by no means universal. The example problem selected here for demonstration was chosen to be convex. This was done to facilitate comparisons with a unique solution—removing the complications arising from iterative methods and multiple local minima in the context of non-convex problems. Even in this simple context of convex problems, the CE method can have tremendous computational advantages over the convex-optimization-based for larger-scale problems such as fluid flows. The semi-definite programming problem underlying Algorithm 4 will scale with $\mathcal{O}(n^6)$ in general. Without a computationally tractable alternative design algorithm, one must begin to consider model reduction (see e.g., [15]). When the problem is non-convex—which is the more realistic case in flow control because the actuation will also be sparse—these computational challenges compound. As such, an efficient heuristic method—such as the CE approach—is most welcome.

Algorithm 4: ***Column-sparse SOF controller design***

Step 1: Compute $\hat{\gamma}$, $\hat{M}$, and $\hat{P}$ by solving the following semi-definite programming problem,

$$\begin{aligned} &minimize \quad \gamma \\ &subject \ \ to \quad \begin{bmatrix} A^T P + PA + MC + C^T M^T & P & M \\ P & -I & 0 \\ M^T & 0 & -I \end{bmatrix} \leq 0 \\ &\begin{bmatrix} \gamma & x_0^T \\ x_0 & P \end{bmatrix} \leq 0 \end{aligned} \tag{B3}$$

where x_0 is the initial condition. An SOF controller gain follows as $F = \hat{P}^{-1} M$ with associated cost $J = \hat{\gamma} = x_0^T \hat{P}^{-1} x_0$.

Step 2: Compute a column-sparse matrix M_{sparse} by solving the same optimization problem in B3 with an additional inequality constraint

$$\gamma \leq \xi J \tag{B4}$$

where $\xi > 1$, but sufficiently small so that the resulting M_{sparse} contains s columns $(M_{s1}, ...M_{ss})$ whose 2-norms are approximately zero.

Step 3: Set the s columns $(M_{s1}, ...M_{ss})$ to zero. The final SOF controller gain is computed as

$$F = P^{-1} M_{sparse} \tag{B5}$$

where F contains zero columns $(F_{s1}, ...F_{ss})$.

Appendix C Grid resolution study

Grid resolution studies have been performed for streamwise- and spanwise-wave disturbances, as shown in Fig. 18. The coarse and refined meshes contain $64 \times 101 \times 64$ and $128 \times 101 \times 64$ grid points in the x-, y- and z-direction, respectively. The grids have been tested using different optimal disturbance amplitudes. At the transient energy growth and laminar-to-turbulent transition stages, the results from the coarse and refined meshes overlap before the flows have completely become turbulent. The results in Fig. 18 indicate that the

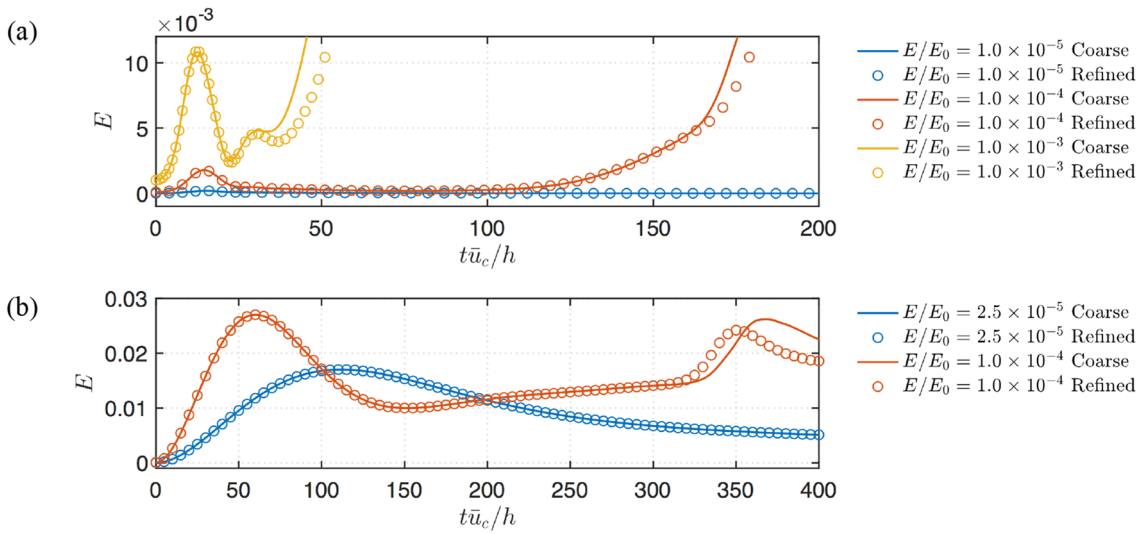

Fig. 18 Grid resolution study of transient kinetic energy density E for **a** streamwise-wave and **b** spanwise-wave disturbance cases

grid resolution is sufficient for the flow condition considered in the present work, which does not require fully resolving the turbulent flow. Because we further examine the transition mechanism in the channel flow, the refined mesh is adopted in the direct numerical simulation to better capture relatively small-scale structures present during the transition process. Moreover, because the flow with oblique-wave disturbance has similar characteristics to the one with streamwise-wave disturbance, the grid selected for streamwise-wave disturbance is sufficient to resolve the flow response to the oblique-wave disturbance.

References

1. Schmid, P.J., Henningson, D.S.: Stability and Transition in Shear Flows. Springer, New York (2001)
2. Schmid, P.J.: Nonmodal stability theory. Annu. Rev. Fluid Mech. **39**(1), 129–162 (2007)
3. Landahl, M.T.: A note on an algebraic instability of inviscid parallel shear flows. J. Fluid Mech. **98**(2), 243–251 (1980). https://doi.org/10.1017/S0022112080000122
4. Farrell, B.F., Ioannou, P.J.: Optimal excitation of three-dimensional perturbations in viscous constant shear flow. Phys. Fluids A **5**(6), 1390–1400 (1993). https://doi.org/10.1063/1.858574
5. Reddy, S.C., Henningson, D.S.: Energy growth in viscous channel flows. J. Fluid Mech. **252**, 209–238 (1993)
6. Trefethen, L.N., Trefethen, A.E., Reddy, S.C., Driscoll, T.A.: Hydrodynamic stability without eigenvalues. Science **261**(5121), 578–584 (1993)
7. Jovanović, M.R., Bamieh, B.: Componentwise energy amplification in channel flows. J. Fluid Mech. **534**, 145–183 (2005)
8. Bamieh, B., Dahleh, M.: Energy amplification in channel flows with stochastic excitation. Phys. Fluids **13**(11), 3258–3269 (2001). https://doi.org/10.1063/1.1398044
9. Butler, K.M., Farrell, B.F.: Three-dimensional optimal perturbations in viscous shear flow. Phys. Fluids A **4**, 1637–1650 (1992)
10. Hemati, M.S., Yao, H.: Performance limitations of observer-based feedback for transient energy growth suppression. AIAA J. **56**(6), 2119–2123 (2018). https://doi.org/10.2514/1.J056877
11. Högberg, M., Bewley, T.R., Henningson, D.S.: Linear feedback control and estimation of transition in plane channel flow. J. Fluid Mech. **481**, 149–175 (2003)
12. Ilak, M., Rowley, C.W.: Feedback control of transitional channel flow using balanced proper orthogonal decomposition. In: 5th AIAA Theoretical Fluid Mechanics Conference (2008)
13. Martinelli, F., Quadrio, M., McKernan, J., Whidborne, J.F.: Linear feedback control of transient energy growth and control performance limitations in subcritical plane Poiseuille flow. Phys. Fluids **23**(1), 014103 (2011)
14. Sun, Y., Hemati, M.S.: Feedback control for transition suppression in direct numerical simulations of channel flow. Energies **12**(21), 4127 (2019)
15. Kalur, A., Hemati, M.S.: Control-oriented model reduction for minimizing transient energy growth in shear flows. AIAA J. **58**, 1034–1045 (2019)
16. Yao, H., Hemati, M.S.: Revisiting the separation principle for improved transition control. In: 2018 Flow Control Conference. AIAA paper (2018)
17. Bewley, T.R., Liu, S.: Optimal and robust control and estimation of linear paths to transition. J. Fluid Mech. **365**, 305–349 (1998)
18. Hœpffner, J., Chevalier, M., Bewley, T.R., Henningson, D.S.: State estimation in wall-bounded flow systems. part 1 perturbed laminar flows. J. Fluid Mech. **534**, 263–294 (2005). https://doi.org/10.1017/S0022112005004210
19. Toivonen, H.T., Mäkilä, P.M.: A descent Anderson-Moore algorithm for optimal decentralized control. Automatica **21**(6), 743–744 (1985). https://doi.org/10.1016/0005-1098(85)90048-2
20. Syrmos, V.L., Abdallah, C.T., Dorato, P., Grigoriadis, K.: Static output feedback: a survey. Automatica **33**(2), 125–137 (1997). https://doi.org/10.1016/S0005-1098(96)00141-0
21. Cao, Y.-Y., Lam, J., Sun, Y.-X.: Static output feedback stabilization: an ILMI approach. Automatica **34**(12), 1641–1645 (1998). https://doi.org/10.1016/S0005-1098(98)80021-6
22. Yao, H., Hemati, M.S.: Advances in output feedback control of transient energy growth in a linearized channel flow. In: AIAA Scitech 2019 Forum. AIAA paper (2019)
23. Whidborne, J.F., McKernan, J.: On the minimization of maximum transient energy growth. IEEE Trans. Autom. Control **52**(9), 1762–1767 (2007). https://doi.org/10.1109/TAC.2007.900854
24. Yao, H., Sun, Y., Mushtaq, T., Hemati, M.S.: Reducing transient energy growth in a channel flow using static output feedback control. AIAA J. (2022). https://doi.org/10.2514/1.J061345
25. Willcox, K.: Unsteady flow sensing and estimation via the gappy proper orthogonal decomposition. Comput. Fluids **35**(2), 208–226 (2006). https://doi.org/10.1016/j.compfluid.2004.11.006
26. Manohar, K., Brunton, B.W., Kutz, J.N., Brunton, S.L.: Data-driven sparse sensor placement for reconstruction: demonstrating the benefits of exploiting known patterns. IEEE Control Syst. Mag. **38**(3), 63–86 (2018). https://doi.org/10.1109/MCS.2018.2810460
27. Manohar, K., Kutz, J.N., Brunton, S.L.: Optimal sensor and actuator placement using balanced model reduction. arXiv pre-print arXiv:1812.01574 (2018)
28. Clark, E., Askham, T., Brunton, S.L., Kutz, J.N.: Greedy sensor placement with cost constraints. IEEE Sens. J. **19**(7), 2642–2656 (2019)
29. Saito, Y., Nonomura, T., Yamada, K., Asai, K., Sasaki, Y., Tsubakino, D.: Determinant-based fast greedy sensor selection algorithm. arXiv pre-print arXiv:1911.08757 (2020)
30. Yamada, K., Saito, Y., Nankai, K., Nonomura, T., Asai, K., Tsubakino, D.: Fast greedy optimization of sensor selection in measurement with correlated noise. arXiv pre-print arXiv:1912.01776 (2020)

31. Natarajan, M., Freund, J.B., Bodony, D.J.: Actuator selection and placement for localized feedback flow control. J. Fluid Mech. **809**, 775–792 (2016). https://doi.org/10.1017/jfm.2016.700
32. Chen, K.K., Rowley, C.W.: H2 optimal actuator and sensor placement in the linearised complex Ginzburg–Landau system. J. Fluid Mech. **681**, 241–260 (2011). https://doi.org/10.1017/jfm.2011.195
33. Oehler, S.F., Illingworth, S.J.: Sensor and actuator placement trade-offs for a linear model of spatially developing flows. J. Fluid Mech. **854**, 34–55 (2018). https://doi.org/10.1017/jfm.2018.590
34. Bhattacharjee, D., Klose, B., Jacobs, G.B., Hemati, M.S.: Data-driven selection of actuators for optimal control of airfoil separation. Theor. Comput. Fluid Dyn. **34**, 557–575 (2020). https://doi.org/10.1007/s00162-020-00526-y
35. McKernan, J., Papadakis, G., Whidborne, J.F.: A linear state-space representation of plane Poiseuille flow for control design: a tutorial. Int. J. Model. Ident. Control **1**(4), 272–280 (2006)
36. Butler, K.M., Farrell, B.F.: Three-dimensional optimal perturbations in viscous shear flow. Phys. Fluids A **4**(8), 1637–1650 (1992). https://doi.org/10.1063/1.858386
37. Whidborne, J.F., Amar, N.: Computing the maximum transient energy growth. BIT Numer. Math. **51**(2), 447–457 (2011)
38. Brogan, W.L.: Modern Control Theory. Prentice Hall, Upper Saddle River (1991)
39. Rautert, T., Sachs, E.W.: Computational design of optimal output feedback controllers. SIAM J. Optim. **7**(3), 837–852 (1997)
40. Lin, F., Fardad, M., Jovanović, M.R.: Design of optimal sparse feedback gains via the alternating direction method of multipliers. IEEE Trans. Autom. Control **58**(9), 2426–2431 (2013). https://doi.org/10.1109/TAC.2013.2257618
41. Polyak, B.T., Khlebnikov, M.V., Shcherbakov, P.S.: Sparse feedback in linear control systems. Autom. Remote. Control **75**(12), 2099–2111 (2014). https://doi.org/10.1134/S0005117914120029
42. Moore, B.: Principal component analysis in linear systems: controllability, observability, and model reduction. IEEE Trans. Autom. Control **26**(1), 17–32 (1981). https://doi.org/10.1109/TAC.1981.1102568
43. Antoulas, A.C.: Approximation of Large-Scale Dynamical Systems. Society for Industrial and Applied Mathematics, Philadelphia (2005). https://doi.org/10.1137/1.9780898718713
44. Laub, A., Heath, M., Paige, C., Ward, R.: Computation of system balancing transformations and other applications of simultaneous diagonalization algorithms. IEEE Trans. Autom. Control **32**(2), 115–122 (1987). https://doi.org/10.1109/TAC.1987.1104549
45. Gibson, J.F., Halcrow, J., Cvitanović, P.: Visualizing the geometry of state space in plane Couette flow. J. Fluid Mech. **611**, 107–130 (2008)
46. Gibson, J.F.: Channelflow: A spectral Navier–Stokes simulator in C++. Technical report, U. New Hampshire (2014). `Channelflow.org`
47. Reddy, S.C., Schmid, P.J., Baggett, J.S., Henningson, D.S.: On stability of streamwise streaks and transition thresholds in plane channel flows. J. Fluid Mech. **365**, 269–303 (1998)
48. Hunt, J.C.R., Wray, A.A., Moin, P.: Eddies, streams, and convergence zones in turbulent flows. In: Proceedings of the Summer Program, pp. 193–208. Center of Turbulence Research (1988)
49. Leibfritz, F., Lipinski, W.: Description of the benchmark examples in compleib 1.0, technical report. Univ. of Trier (2003). www.complib.de